3-2021

Real-time Aerial Magnetic and Vision-aided Navigation

Daniel J. Clarke

REAL-TIME AERIAL MAGNETIC AND VISION-AIDED NAVIGATION

THESIS

Daniel J Clarke, Captain, USAF

AFIT-ENG-MS-21-M-022

DEPARTMENT OF THE AIR FORCE
AIR UNIVERSITY

AIR FORCE INSTITUTE OF TECHNOLOGY

Wright-Patterson Air Force Base, Ohio

AFIT-ENG-MS-21-M-022

REAL-TIME AERIAL MAGNETIC AND VISION-AIDED NAVIGATION

THESIS

Presented to the Faculty

Department of Electrical and Computer Engineering

Graduate School of Engineering and Management

Air Force Institute of Technology

Air University

Air Education and Training Command

in Partial Fulfillment of the Requirements for the

Degree of Master of Science in Electrical Engineering

Daniel J Clarke, B.S.M.E.

Captain, USAF

March 25, 2021

AFIT-ENG-MS-21-M-022

REAL-TIME AERIAL MAGNETIC AND VISION-AIDED NAVIGATION

THESIS

Daniel J Clarke, B.S.M.E.
Captain, USAF

Committee Membership:

Maj Joseph A. Curro, Ph.D
Chair

Dr. Robert C Leishman, Ph.D
Member

Maj Aaron J. Canciani, Ph.D
Member

Abstract

The dependence on Global Positioning System (GPS) by the U.S. military and the vulnerabilities that exist have stressed the need for alternative navigation techniques. Alternative navigation methods must not only approach the accuracy of GPS but also the world-wide availability. Vision-aided navigation systems that provide absolute positioning estimates have demonstrated encouraging results that approach the level of accuracies seen with GPS. They are however, limited over oceans and other areas of feature-less terrain. Magnetic navigation using the Earth's magnetic anomaly field has proven to be a promising alternative that can provide world-wide coverage for a navigation system. This research demonstrates the combination of a magnetic and vision-aided navigation system using an extended Kalman filter (EKF) to aid an aircraft's inertial navigation system (INS). Using synthetic magnetic field measurements and flight test computer vision data, it is shown that magnetic navigation can bound the navigation solution to a coarse position estimate during long outages of computer vision data. Once computer vision data is available, the vision-aided navigation system is able to initialize using the coarse position estimate and then provide an under 10 meter accuracy solution, near GPS level accuracy. Additionally, this research demonstrates a limited magnetic compensation method and magnetic navigation on F-16 flight test data. Limited compensation is able to reduce the 10,000 nano-Teslas (nT) disturbance field of the F-16 to approximately 15 nT. The compensated data is then successfully used for magnetic navigation. A bounded navigation solution is obtained achieving accuracies on the order of 100 meters with a navigation grade INS and on the order of 1,000 meters with a tactical grade INS.

Table of Contents

Page

List of Figures

List of Tables

REAL-TIME AERIAL MAGNETIC AND VISION-AIDED NAVIGATION

I. Introduction

1.1 Problem Background

The Global Positioning System (GPS) is the premier navigation system used by U.S. civilian and military platforms alike. It is a world-wide available system and receivers are entirely passive systems (they do not emit energy that can be detected). It has become increasingly used by the U.S. military since its inception. GPS is also highly susceptible to jamming or spoofing. Multiple military strategy documents have stressed the need for alternative navigation techniques. Two techniques that have shown great promise are magnetic navigation and vision-aided navigation.

1.1.1 Magnetic Navigation

Magnetic navigation uses scalar intensity measurements or vector measurements of the Earth's magnetic anomaly field and a reference map (or maps) of the magnetic anomaly field to estimate position and aid inertial measurements. Similar to GPS, the Earth's magnetic anomaly field is available world-wide, including over the oceans, and magnetic field sensors are entirely passive. The Earth's magnetic field is always available, but it is much less susceptible to jamming. Previous research by Canciani in [1] shows navigation results approaching 10 meter level accuracy in an ideal environment. The research was tested on a magnetically "clean" geo-survey aircraft optimized for measuring the Earth's magnetic anomaly field, and it was flown at a low and constant altitude over a near perfect anomaly map. In a non-ideal environ-

ment, such as on an operational aircraft, magnetic navigation becomes much more challenging and GPS level accuracy is more difficult to achieve. Despite possible degraded navigation accuracy on an operational aircraft, magnetic navigation shows promise in providing a less accurate world-wide navigation solution in the absence of GPS. The less accurate solution could bound the position error drift that would typically be seen in a drifting inertial navigation system (INS) only navigation solution. This research explores using magnetic navigation on an operational platform combined with a vision-aided navigation system.

1.1.2 Vision-Aided Navigation

Vision-aided navigation uses aerial imagery and computer vision software to aid inertial measurements. An absolute positioning vision-aided system uses computer vision to match features between two images and estimate position. Features extracted from real-time imagery are compared to a reference set of images of the same area. Computer vision algorithms are able to take matching features between the two sets of images and extract an estimate of the aircraft position. A vision-aided navigation system is another passive system, but it is not available world-wide. It is only available where aerial images with recognizable features can be recorded—over the oceans it is not available. However, vision-aided navigation is a much more compelling system to achieve GPS level accuracy when it is available. Previous research by Venable in [2] shows navigation results approaching GPS level accuracy. This research explores using a vision-aided navigation system combined with a magnetic navigation system to achieve a world-wide available navigation solution with near GPS level accuracy.

1.2 Research Objectives and Contributions

There are two research areas explored in this thesis. First, a magnetic and vision-aided navigation system capable of running in real-time is tested. Synthetic magnetic field measurements are added to flight test computer vision (aerial imagery) and inertial measurement unit (IMU) data, and a simulation is run with real-time playback. This simulation will demonstrate magnetic and vision-aided navigation working together. It will demonstrate a vision-aided navigation system initializing off of a magnetic navigation solution. Additionally, it will demonstrate a bounded magnetic navigation solution during periods of time with computer vision outages.

Second, a limited demonstration of magnetic navigation is conducted on an F-16 with flight test magnetic field data. The demonstration will explore whether magnetic navigation can bound the navigation solution on a dynamic and operational aircraft—a more challenging environment than the ideal conditions seen in previous magnetic navigation testing. While compensation of large magnetic field disturbances (as seen on the F-16) is one of the most challenging aspects of magnetic navigation, it is not a focus of this research. A limited approach to compensation is completed, simply as an intermediary step to obtain magnetic navigation results on the F-16.

This research will present the first demonstration of a combined magnetic and vision-aided navigation system. It required the development of a magnetic navigation system in The Air Force Institute of Technology's (AFIT's) plug and play navigation framework called Scorpion. This development is a starting point for a fully operational magnetic navigation system within the plug and play framework. The results of the combined magnetic and vision-aided navigation simulations will provide examples for the benefits of combining the two navigation systems to use as an alternative to GPS.

Additionally, this research is the first to analyze and show that magnetic navigation is possible on a fighter-type aircraft, outside of initial analysis done in the flight

test report. The F-16 flight testing executed for this research is the first magnetic field data set recorded on an Air Force operational platform. This abundant data set can be used for future work on improving magnetic compensation methods for large aircraft disturbances and for improving magnetic navigation algorithms.

1.3 Thesis Overview

This thesis is organized into five chapters. Chapter I provides an introduction to magnetic and vision-aided navigation as an alternative to GPS and provides motivation and contribution to the research presented.

Chapter II provides background information on magnetic navigation and vision-aided navigation, including an overview of previous and related work. Concepts required for magnetic navigation and vision-aided navigation are presented to the reader, along with a brief background on the navigation filtering. Chapter III details the methodology used to conduct this research. First the simulation methods for testing combined magnetic and vision-aided navigation are discussed. Then the methods used to analyze flight test F-16 magnetic field data are detailed. Chapter III also provides an overview of the data sets used to complete this research. Chapter IV presents the results and analysis on this research. Simulation and F-16 magnetic navigation results are discussed and notable results are detailed. Finally, Chapter V concludes the thesis by summarizing key results from Chapter IV and discussing important conclusions based on thesis objectives. Considerations for future work are presented based on the findings from this research.

II. Background and Literature Review

This chapter provides the reader with a background on aerial magnetic navigation and vision-aided navigation, including an overview of previous and related work. Section 2.1 details using the Earth's magnetic anomaly field for aerial magnetic navigation. Recent work is discussed along with information pertinent to understanding and designing an aerial navigation system. Section 2.2 provides an overview of vision-aided navigation. Concepts required for a vision-aided navigation system that provides an absolute position estimate will be detailed. Section 2.3 covers the extended Kalman filter (EKF) and Section 2.4 covers the 15 state Pinson inertial navigation system (INS) error model. Lastly, Section 2.5 highlights the Air Force Institute of Technology (AFIT)'s Scorpion navigation framework which provides a plug-and-play navigation utility for the development and execution of this research.

2.1 Aerial Magnetic Navigation

Aerial magnetic navigation uses the Earth's magnetic anomaly field—anomalies from the Earth's crustal magnetic field—as a navigation signal to estimate position and aid aircraft inertial measurements. The anomaly field is available world-wide at all times, including over oceans. Sensors for measuring the magnetic field are generally low in size, weight, and power, and are passive devices. Additionally, magnetic fields are much less susceptible to jamming or spoofing than electromagnetic signals. These characteristics show promise for magnetic navigation's use as an alternative navigation method when Global Positioning System (GPS) is unavailable. Limited experimental results on magnetic navigation in an aerial environment were available in [3] until Canciani's work in *Absolute Positioning Using the Earth's Magnetic Anomaly Field* [1]. Canciani presented a navigation filter that utilizes scalar magnetic intensity

measurements of the Earth's anomaly field to aid an aircraft's INS. The filter compares the anomaly field measurements to a map of anomaly field values using a marginalized particle filter. They were able to demonstrate navigation accuracy of 13 meters Distance Root Mean Square (DRMS) with real flight data in ideal conditions [1]. The ideal conditions for this experiment were as follows:

- The flight was conducted in level flight at a low altitude over land.
- The reference magnetic anomaly map was of high-quality.
- A navigation-grade INS was used.
- A magnetically clean aircraft was used.

Canciani's work motivated further research into magnetic navigation as an alternative navigation method. In [4], magnetic navigation was tested in level flight over the ocean where the effective aircraft height above the Earth's crust is higher. Experiments were conducted with a high-quality anomaly map using both fully-sampled and under-sampled data. The under-sampled map effectively lowers the quality of the map. With a fully-sampled map, they were able to demonstrate navigation accuracy on the order of tens of meters using a navigation-grade INS. With the under-sampled map, they were able to demonstrate accuracies on the order of a few hundred meters using a navigation-grade INS [4].

In [5], magnetic navigation simulations experimented with water-based ship trajectories using vector and tensor measurements of the Earth's anomaly field instead of scalar intensity measurements. In these experiments, an EKF was used instead of a particle filter. The simulations demonstrated navigation accuracy of 35 meters DRMS for a one-hour ship trajectory. These results were obtained with tensor measurements and a navigation-grade INS [5].

Another notable magnetic navigation experiment was conducted in [6], where a simultaneous localization and mapping (SLAM)-based method for magnetic navigation was investigated. SLAM techniques would allow magnetic navigation to be flown without the use of magnetic anomaly maps as reference. Real flight data was gathered on a low-flying commercial off-the-shelf (COTS) unmanned aerial vehicle (UAV), and demonstrated navigation accuracy on the order of tens of meters using three different grades of INS [6].

This research continues off work done by Canciani in [1]. The following subsections on aerial magnetic navigation closely follow Canciani [1]. They will provide the reader with a limited geo-physics background on the Earth's magnetic field. Only information that is pertinent to understanding and designing an aerial navigation system will be discussed.

2.1.1 Earth's Magnetic Field

The Earth's magnetic field consists of both internal and external sources, shown in Figure 1. These sources contribute to three of the four main measurable components for aerial navigation: The core field, crustal field, and space weather effects. The fourth component, aircraft effects, are discussed in further detail in Section 2.1.4.

Core Field

The Earth's core field, or main field, is generated by electromagnetic currents of the liquid iron core deep within the Earth. It accounts for roughly 98% of Earth's measured magnetic field [8]. This field is what most people are familiar with; it makes a compass point North. It can be approximated by a magnetic dipole aligned along the earth's axis of rotation.

The average magnitude of the main field is about 50,000 nT and it varies by

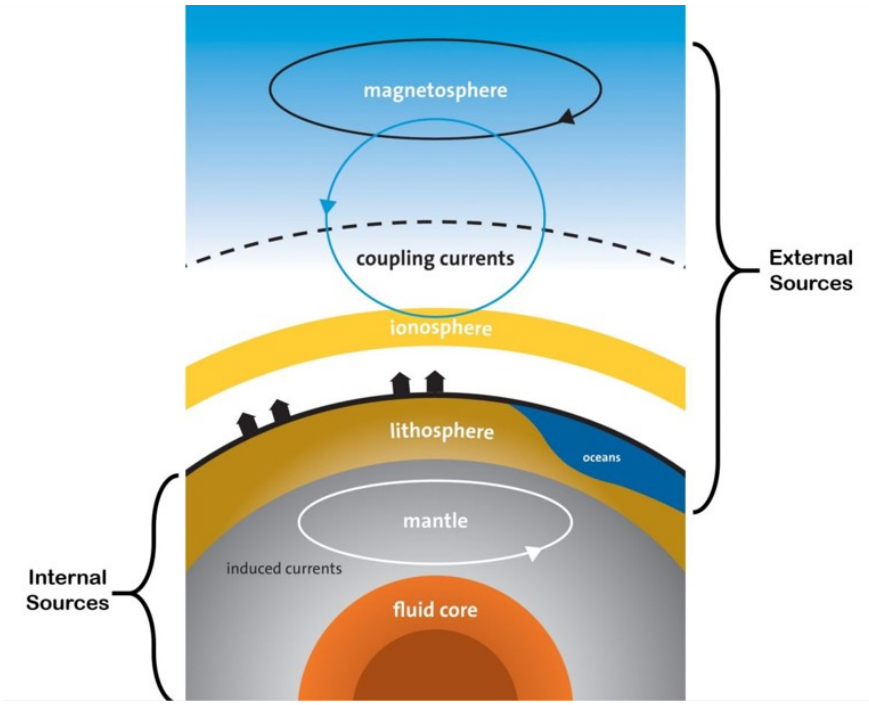

Figure 1: Earth's magnetic field sources [7].

approximately ± 20,000 nT based on your global location [9]. It is well-modeled by reference systems such as the World Magnetic Model (WMM). The field undergoes secular variations over long periods of time. These variations are not insignificant, so the field is remodeled every five years to account for observed changes [10]. The spatial wavelengths associated with the main field are on the order of thousands of kilometers. Figure 2 shows how little spatial variation there is in this field. A low frequency signal such as this is unsuitable for navigation [10].

Crustal Field

The Earth's crustal field, or lithosphere field, is caused by permanent or induced magnetization of rocks in the Earth's crust. It accounts for approximately 1-5% of Earth's measured magnetic field with a magnitude on the order of 100s of nano-Teslas [12].

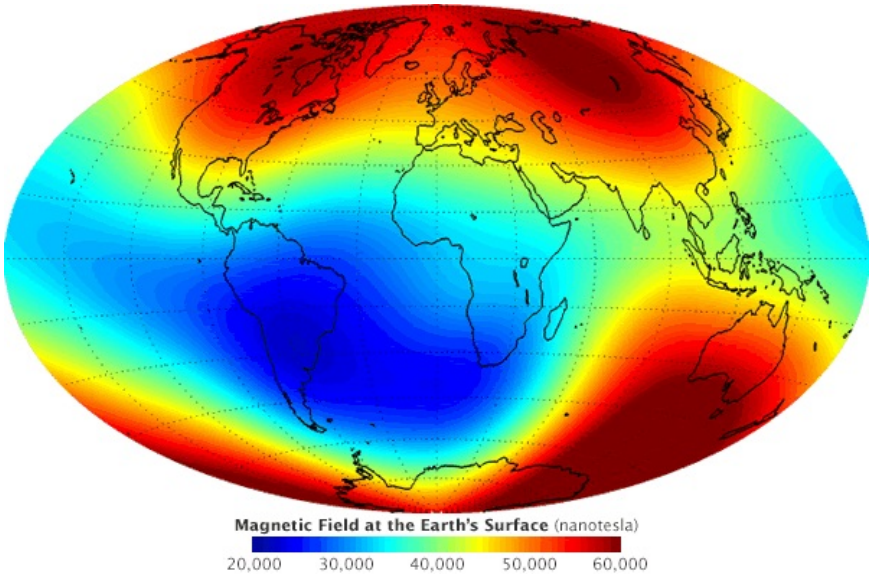

Figure 2: Earth's main field at Earth's surface [11].

In contrast to the main field, there are two important aspects of the crustal field that make it an ideal candidate for navigation. Firstly, the crustal field changes so slowly over time that it can be considered static on geological time scales. This implies that maps of the field are valid for many decades. Secondly, the crustal field includes high spatial frequency information [1]. The world-wide variation in this field is well-shown in Figure 3, which displays the Earth Magnetic Anomaly Grid (EMAG) [13].

Space Weather Effects

Space weather effects is an all-encompassing term for the time-varying, unpredictable fields in the environment that corrupt magnetic measurements. These do not include aircraft effects. They are more formally referred to as "temporal variations", because they primarily consist of the temporal variations originating in the ionosphere and magnetosphere. Additional contributions are from ocean currents, coupling currents, and induced currents in the mantle among others [1]. Not only are

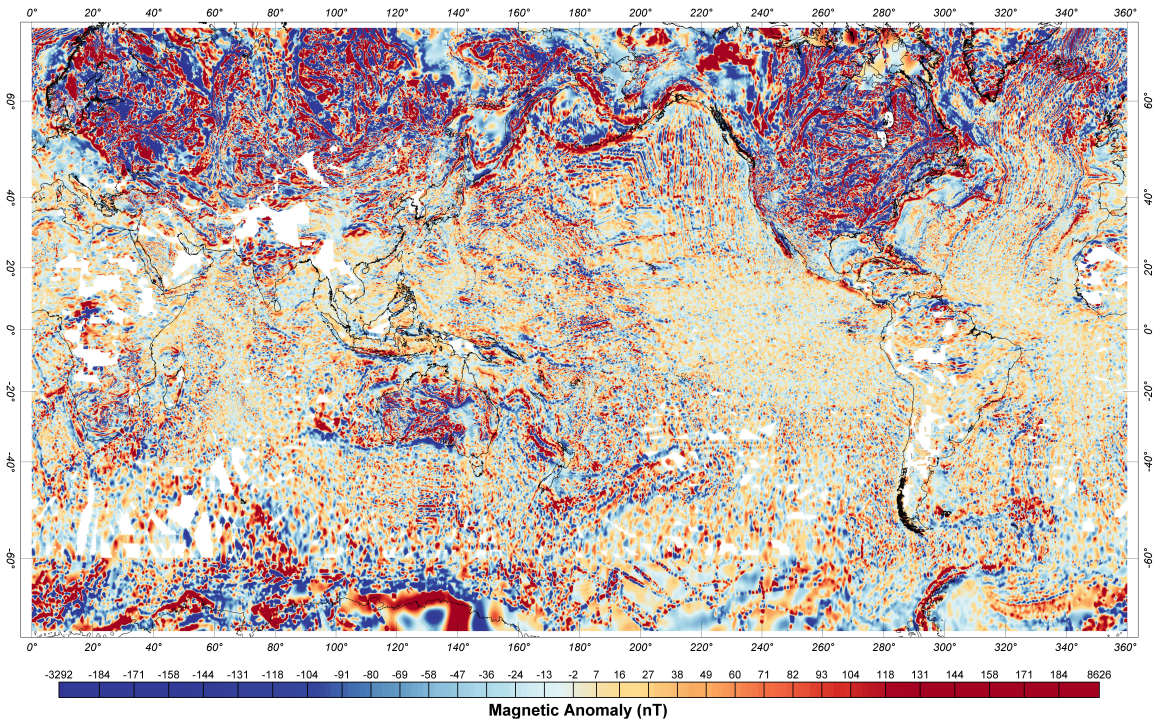

Figure 3: Earth's crustal field at 4 km altitude, EMAG2 version 3 [14].

they time-varying, but they are highly dependent on location as well. The magnitude of temporal variations are weak compared to the main field and crustal field. Typically, the daily cycle for these variations are on the order of 10s of nano-Teslas [9]. Figure 4 shows 24 hours of temporal variations collected at four different base stations in the Western United States. This plot depicts the similarities in the low-frequency spectrum of the variations. It can be implied that at low frequencies the temporal variations are consistent over a regional area.

World Magnetic Model

The WMM is the standard core field model used by the United States Department of Defense for navigation using the Earth's geomagnetic field [16]. The model primarily characterizes the core field and includes its rate of change to account for secular variations. Unpredictable changes in the core field over time require the model to

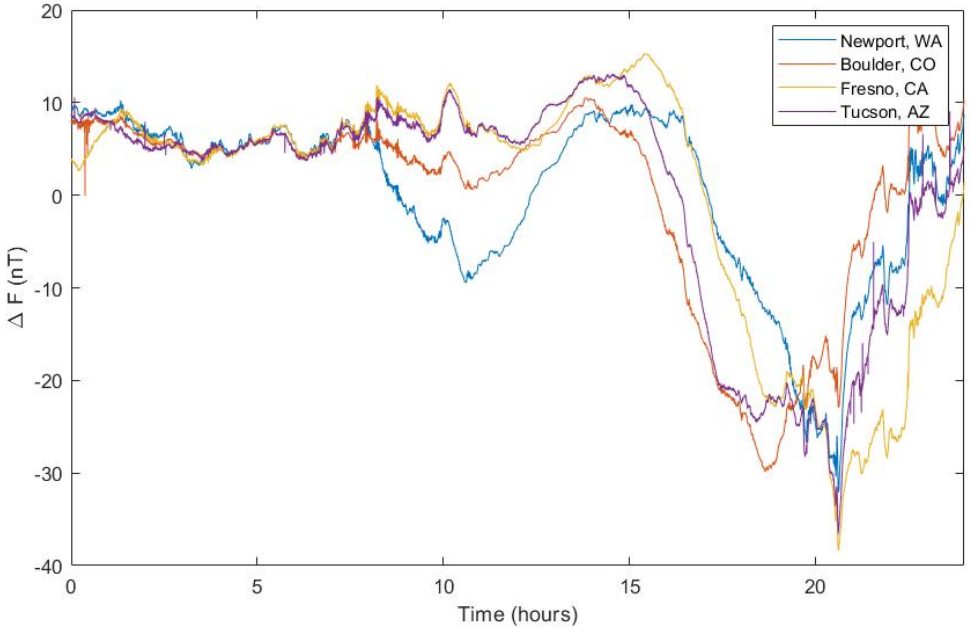

Figure 4: Temporal Variations with mean removed over a 24 hour period at different base stations in the Western United States. Figure generated from data provided by [15]

be updated and released every five years by the National Centers for Environmental Information (NCEI) on behalf of the National Geospatial-Intelligence Agency (NGA) [16]. The WMM can be used as a reference field for the Earth's main field when processing aeromagnetic field data for navigation. The expected Earth main field can be computed based on latitude, longitude, altitude, date, and time.

2.1.2 Earth's Magnetic Anomaly Field

A magnetic anomaly is the scalar deviation from a reference field. The reference field for our purposes is the main Earth field, and the anomalies of interest come from Earth's crustal field [1]. Magnetic anomaly maps have been generated for decades in order to study the Earth's subsurface. This valuable information is commonly used in industry for resource mining and drilling. Large joint efforts have been conducted to produce magnetic anomaly map data for entire continents. The North American

Magnetic Anomaly Database (NAMAD) is one example of those efforts, and is one of the anomaly maps used in this research. Furthermore, the creation of anomaly maps and using them for navigation requires the use of map transforms. One type of transform, continuation filters, allow two-dimensional anomaly maps to be accurately projected into three dimensions.

Anomaly Definition

Consider the total magnetic field intensity (B_{total}) to be the vector summation of the main Earth field (B_{main}) and the magnetic anomaly created by the Earth's crustal field ($B_{anomaly}$), as shown in (1).

$$B_{total} = B_{main} + B_{anomaly} \tag{1}$$

We can approximate the magnitude of the magnetic anomaly by performing scalar subtraction between the magnitude of the total field and the magnitude of the main Earth field, shown in (2).

$$\|B_{anomaly}\| \approxeq \|B_{total}\| - \|B_{main}\| \tag{2}$$

This approximation is only valid when $\|B_{main}\| \gg \|B_{anomaly}\|$. The main field is on the order of 50,000 nT and the crustal anomaly field is on the order of 100 nT. More appropriately stated, a scalar magnetic anomaly represents an approximation to the

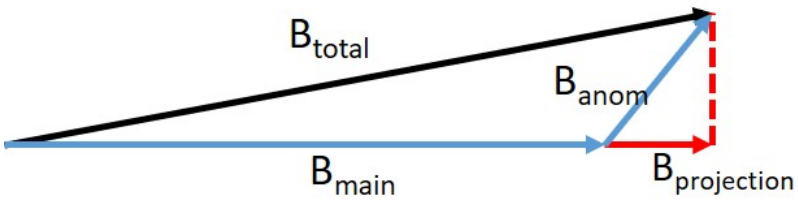

Figure 5: Projection of magnetic anomaly onto the main Earth field.

projection of the magnetic anomaly along the reference field direction [1]. Figure 5 illustrates this vector projection. The length of the anomaly vector is exaggerated for reader visibility.

Scalar Magnetic Anomaly Maps

Magnetic anomaly navigation is a map-based navigation system [1]. Scalar magnetic anomaly maps are comprised of a geolocated grid of scalar magnetic measurements intended to capture only the intensity of the Earth's crustal field [4]. When maps are created, the same assumptions as above hold. What is mapped is the actual scalar subtraction ($B_{total} - B_{main}$). It is approximately equal to the projection of the magnetic anomaly onto the main Earth field.

Maps are typically created by flying gridded survey lines at constant altitude above ground level and measuring the scalar magnetic field intensity. Altitude may also be flown at a constant mean sea level. The main Earth field is removed from the measurements using a reference field. Temporal variations are removed by use of base station measurements[9]. The geomagnetic survey (geo-survey) aircraft used are magnetically quiet, and sensors are placed in advantageous positions away from large magnetic disturbances on the aircraft. Magnetic compensation is still performed to remove what little remaining aircraft disturbance field exists [1]. Aircraft magnetic compensation will be further discussed in Section 2.1.5.

Two important factors for magnetic anomaly maps are line spacing and altitude. The line spacing is the spacing between survey lines. It is driven by the desired resolution of the map, as well as the altitude. Flying at a line spacing equal to the survey height ensures the map is fully sampled—all spatial frequencies in the magnetic anomaly signal are captured [17]. Knowing whether a map is fully sampled, or close to fully sampled, is important for magnetic navigation. It ensures the correct

reconstruction of the signal when interpolating [1]. This ability to fully reconstruct the signal from a gridded map is a unique advantage of magnetic navigation over other map-based navigation systems [1].

The altitude of the magnetic anomaly map is important not only because it is a driving factor for your line spacing. The Earth's magnetic field is a three dimensional field, meaning intensity values for the measured field change with altitude. Increasing altitude essentially acts as a low pass filter [1]. Intuitively, flying low altitude surveys will lead to a higher map resolution. As altitude increases, a "blurring" effect is seen in the magnetic intensity data as high-frequency components are reduced. This indicates that for magnetic navigation, altitude will have a large impact on navigation performance.

North American Magnetic Anomaly Database

The NAMAD is the result of a joint effort by the Geological Survey of Canada (GSC), United States Geological Survey (USGS), and Consejo de Recursos Minerales of Mexico (CRM) [18]. The magnetic anomaly data for the entirety of North America is shown in Figure 6. It is a collection of decades of magnetic anomaly maps collected a pieced together into one large database. With individual maps dating back to the 1980s, the database almost completely covers North America [18].

Using the NAMAD as a navigation aid is prevented by three primary error sources [1]:

1. Some map data is poorly geolocated,
2. Majority of the map is undersampled, and
3. Areas of the map are missing data entirely

Poor geolocation of some of the map data is caused by the maps being collected

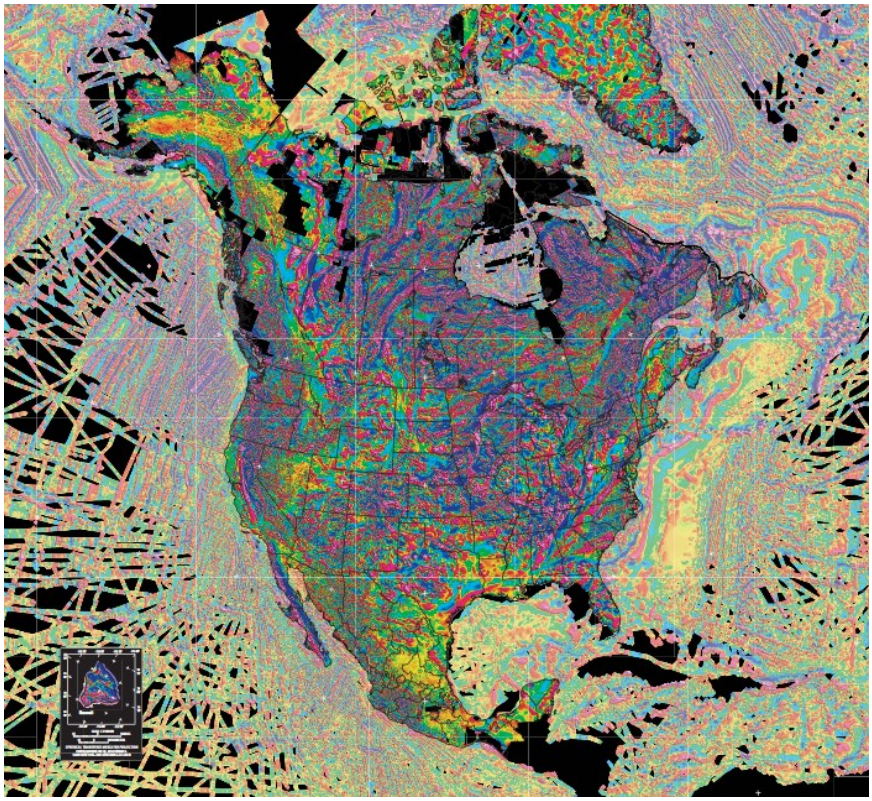

Figure 6: North American Magnetic Anomaly Map, 1km grid spacing at 305 meter altitude [18].

prior to GPS being readily available. This can cause location errors in the map up to hundreds of meters [1]. The map is technically at an altitude of 305 meters above terrain, but is very under-sampled at this altitude [1]. Some maps used for the database were sampled at upwards of 8 km line spacing [18]. Lastly, some data is missing altogether. This is particularly true over the oceans and some coastal regions.

The NAMAD can still prove useful for magnetic navigation. Flying at higher altitudes, the NAMAD can be used as an accurate reference. Additionally, it has proven to be a useful tool for simulating magnetic measurements, which was done in this research.

Continuation Filtering

Magnetic anomaly maps exist in two-dimensions with a constant altitude. When using a map as a reference for map-based navigation, transforms such as continuation filtering are required to create a three-dimensional map of magnetic anomaly values. Specifically, upward continuation is used to create magnetic anomaly maps at altitudes higher than a known two-dimensional map of surveyed magnetic anomaly values.

Magnetic anomaly fields are potential fields. Upward continuation is used to calculate the potential field at any point above a known potential field [19]. The upward continuation integral is derived from Laplace's equations and Green's identities in [19] and is given by

$$U(x, y, z_0 - \Delta z) = \frac{\Delta z}{2\pi} \int_{-\infty}^{\infty} \int_{-\infty}^{\infty} \frac{U(x', y', z_0)}{\left[(x - x')^2 + (y - y')^2 + \Delta z^2\right]^{3/2}} \delta x' \delta y'. \quad (3)$$

The use of the upward continuation integral is computationally expensive. An equivalent expression in the Fourier domain is derived in [19]. More details on the use of upward continuation and the Fourier domain algorithm can be found in [1] and [19].

2.1.3 Magnetic Measurements and Sensors

Two types of magnetic measurements are required for scalar magnetic anomaly navigation: Scalar measurements and vector measurements. Scalar measurements are used to obtain the navigation signal and vector measurements are used in compensation of aircraft effects.

Scalar Measurements and Sensors

Magnetic fields are vector fields consisting of both direction and magnitude. Scalar measurements capture only the total intensity, or magnitude, of a surrounding magnetic field. Ideally, a scalar magnetic intensity measurement would be constant at a given point in time and space, independent of the orientation of the measurement device.

Scalar magnetometers are the devices used to obtain scalar measurements. Modern scalar magnetometers have accuracies on the order of 1 nano-Tesla and sensitivities on the order of pico-Teslas [8].

When using a scalar magnetic anomaly map as reference for navigation, scalar magnetometers are the main measurement device used to obtain the navigation signal. As mentioned above, a scalar measurement consists of the total intensity of a surrounding magnetic field. In the flight environment, a scalar measurement includes corrupting magnetic fields beyond the Earth's anomaly field which will be discussed in Section 2.1.4.

Vector Measurements and Sensors

Vector measurements can directly measure the components of a surrounding magnetic field. Both magnitude and direction information are obtained with these measurements. The magnitude, $\mathbf{B}$ is given by

$$\mathbf{B} = \sqrt{B_x^2 + B_y^2 + B_z^2}, \tag{4}$$

where B_x, B_y, and B_z are the individual components of the surrounding magnetic field. The components are oriented along the axes of the vector measurement device.

Vector magnetometers are the devices used to obtain vector measurements. Vector magnetometers are much less accurate than scalar magnetometers, and have worse

performance at the low frequencies needed for magnetic navigation [1].

For navigation using a scalar magnetic anomaly map, vector magnetometers can be used for some forms of aircraft magnetic compensation. Although they are low in accuracy compared to scalar magnetometers, they allow for the observation of magnetic field changes based on aircraft orientation. This concept is used in aircraft magnetic compensation, further described in Section 2.1.5. In a flight environment, vector measurements include the same corrupting magnetic fields as scalar measurements.

2.1.4 Measuring the Magnetic Anomaly Field in a Flight Environment

The Earth's magnetic anomaly field, the navigation signal for magnetic navigation, is not directly measurable in flight. It can however be isolated from scalar magnetic intensity measurements. Scalar magnetic intensity measurements measure total magnetic intensity of the surrounding magnetic field. There are four main components in the total magnetic intensity in a flight environment.

1. Earth's Anomaly Field
2. Earth's Main Field
3. Aircraft Disturbance Field
4. Space Weather Effects

Non-anomaly field components can be thought of as measurement errors, or corrupting sources [1]. Fortunately, there are methods for removing these corrupting sources from the total magnetic intensity.

Earth's Main Field

The easiest corrupting source to remove is the Earth's main field. As discussed previously, the Earth's main field has an average magnitude of about 50,000 nT and varies by approximately ± 20,000 nT based on your global location [9]. Since it is well-modeled by reference systems such as the WMM, it can be removed from the total magnetic intensity using the model and an estimate of current aircraft position and time.

Aircraft Disturbance Field

By far the most challenging corrupting source to remove is the aircraft disturbance field. This field is the disturbance to the Earth's magnetic field that is caused by the aircraft and field generated by the aircraft itself. It is caused primarily by magnetically susceptible materials on the aircraft and their orientation within the Earth's magnetic field [9]. Additionally, aircraft systems and electronics can cause disturbance depending on their size, power, function, and relative location to the magnetometers being used.

Permanent magnetization, induced magnetization, and eddy currents are three sources of disturbance caused by magnetically susceptible materials on the aircraft. The aircraft's permanent field is caused by actual magnetic components of the aircraft. This field is a relatively constant magnitude in relation to the aircraft, but it's direction changes with the aircraft attitude [9]. The induced aircraft field is caused by the magnetically susceptible materials of an aircraft flying in an external magnetic field, the Earth's magnetic field [1]. The orientation of the aircraft within the Earth's magnetic field is a large contributor to both the magnitude and direction of the aircraft's induced magnetic field. Eddy currents are electrical currents running through conductive materials on the aircraft. These electrical currents are caused by conduc-

tive material moving within an external magnetic field according to Faraday's law of induction. The Eddy currents create their own corrupting magnetic field following the Bio-Savart law [1], which describes the magnetic field generated by an electric field.

Aircraft systems and electronics can cause corrupting magnetic fields following similar principles as those described above. Some systems function by causing magnetically susceptible material to displace: Moving control surfaces, actuators, and fuel or hydraulic pumps. Other systems consist of high power electrical systems: Communications, RADAR, and lighting. These examples are not all inclusive, but can give the sense of just how many systems there can be on a modern operational aircraft. Each system has the potential to contribute to the aircraft disturbance field depending on their proximity to magnetometers.

The primary and preferred method for removing or reducing the aircraft disturbance field is to place magnetometers as far away from disturbance causing sources as possible. Geo-survey aircraft typically use a "stinger" to place the magnetometers far away from the aircraft engines, their main source of induced disturbance. Figure 7 shows a tail-mounted stinger on a geo-survey aircraft. When the magnetometers are in a stinger, the aircraft disturbance field is typically under 10 nT [9]. When the magnetometers are not placed far away from corrupting sources, disturbance field values can be thousands of nano-Teslas or greater. This will most likely be the case for currently fielded operational aircraft that were not designed around the aspects of magnetic navigation; however, magnetometer placement must still be studied and considered as it is by far the most effective means of reducing the aircraft disturbance field.

To further reduce the aircraft disturbance field, aircraft magnetic compensation systems can estimate and remove the aircraft magnetic fields based on the orientation

Figure 7: Tail-mounted stinger on a geo-survey aircraft [20].

of the aircraft within the Earth's magnetic field [1]. Additionally, compensation systems can potentially incorporate other known and observable corrupting sources (i.e. aircraft systems and electronics) into the estimation methods. This research field is rapidly expanding and is not a focus of this paper. Further reading can be done in [21] and [22]. Section 2.1.5 provides an introduction to traditional aircraft compensation methods used in previous research on magnetic navigation.

Space Weather Effects

The final corrupting source to remove from total magnetic intensity is space weather effects. As described in Section 2.1.1, space weather effects consist primarily of temporal variations. Traditionally, geomagnetic surveyors will remove temporal variations by using magnetic base stations located nearby the magnetic survey (less than approximately 100 km). Any variations recorded by a static base station (isolated from nearby environmental effects) can be attributed to temporal variations [1]. This method would not be realistic in real-time flight. Canciani showed that a navigation filter can effectively co-estimate the variations along with position, and remove them from the measured magnetic field. The high-frequency variations are

treated as white noise of zero mean. The low-frequency variations are modeled as a first-order Gauss Markov (FOGM) process [1].

Corrupting Sources Summary

The three main corrupting sources of magnetic fields in a total magnetic intensity measurement are the Earth's main field, aircraft disturbance field, and space weather effects. Methods exist, or are under further development, to remove these corrupting sources from the measurement in real-time and are important in isolating the Earth's magnetic anomaly field in flight. The importance of their removal can be seen by their relative magnitude compared to the magnitude of the Earth's anomaly field. Table 1 summarizes their approximate magnitudes.

2.1.5 Aircraft Magnetic Compensation

Aircraft magnetic compensation consists of methods to model and remove the aircraft disturbance field from the total magnetic field measured in flight. Compensation is necessary to obtain accurate measurements of the Earth's magnetic anomaly field. Traditional compensation methods have been around since the 1950s and have proven effective for geo-survey aircraft and other very low disturbance vehicles. Methods for improving or replacing traditional compensation methods is required for aircraft with large disturbance fields. Aircraft magnetic compensation is a rapidly expanding re-

Table 1: Approximate magnitudes of scalar magnetic intensity measurement components in flight.

Measurement Component	**Approximate Magnitude**
Anomaly Field	0 - 200 nT
Main Field	30,000 - 70,000 nT
Disturbance Field	10 nT (Geo-survey) 10,000 nT (F-16)
Space Weather Effects	0 - 20 nT

search field and is not a focus of this paper.

Traditional Compensation and Tolles-Lawson

Traditional compensation of the aircraft disturbance field primarily uses the Tolles-Lawson model and an in-flight calibration procedure. The disturbance field is estimated and removed using 18 calibration coefficients and vector magnetometer measurements, which are used to observe the orientation of the aircraft within the Earth's magnetic field [1]. The in-flight calibration procedure consists of flying a square pattern and performing a set of pitch, roll, and yaw attitude changes on each leg of the square. The procedure is typically flown at a high altitude over an area of low magnetic anomaly variations. This ensures that there will be little change in the Earth's magnetic field during the procedure, and any variation in the measurements is from the aircraft's attitude changes [9]. Figure 8 shows a depiction of an in-flight calibration procedure with the corresponding scalar magnetic intensity measurement. The variation in the measurements from aircraft attitude changes is used to resolve the calibration coefficients, which can be used to estimate the aircraft disturbance field for the remainder of the flight or on subsequent flights.

The Tolles-Lawson model is given by [24] and [25]. It incorporates effects from the permanent field, induced field, and eddy currents of the aircraft disturbance field, as shown in (5). There are 3 permanent field coefficients, 6 induced field coefficients, and 9 eddy current coefficients.

$$B_{dist} = B_{permanent} + B_{induced} + B_{eddy}, \tag{5}$$

where

$$B_{permanent} = a_1 \cos X + a_2 \cos Y + a_3 \cos Z, \tag{6}$$

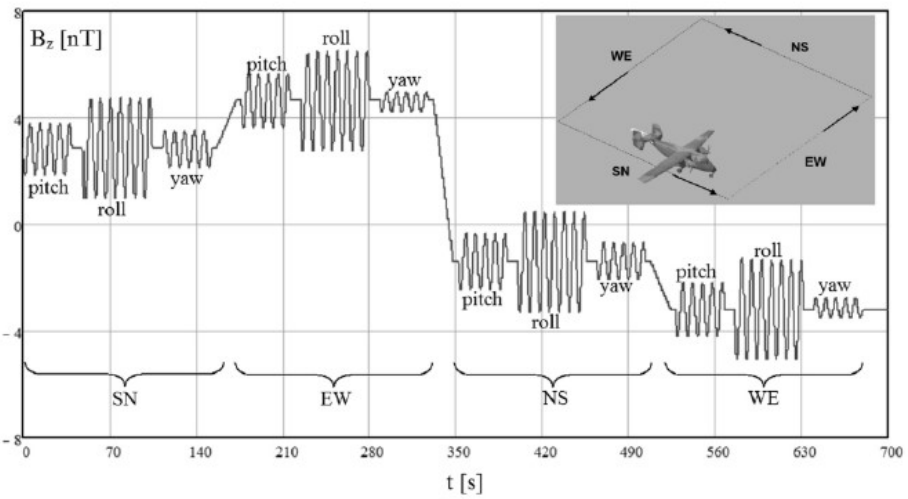

Figure 8: Depiction of in-flight calibration procedure and example magnetic intensity measurement [23].

$$B_{induced} = B_t(a_4 + a_5 \cos X \cos Y + a_6 \cos X \cos Z + a_7 \cos^2 Y + a_8 \cos Y \cos Z + a_9 \cos^2 X), \tag{7}$$

$$B_{eddy} = B_t(a_{10} \cos X \cos \dot{X} + a_{11} \cos X \cos \dot{Y} + a_{12} \cos X \cos \dot{Z} + a_{13} \cos Y \cos \dot{X} + a_{14} \cos Y \cos \dot{Y} + a_{15} \cos Y \cos \dot{Z} + a_{16} \cos Z \cos \dot{X} + a_{17} \cos Z \cos \dot{Y} + a_{18} \cos Z \cos \dot{Z}). \tag{8}$$

B_t is the total magnetic intensity measurement (scalar magnetometer) and the derivatives in (8) are with respect to time. a_{1-18} are the Tolles-Lawson calibration coefficients. $\cos X$, $\cos Y$, and $\cos Z$ are direction cosine terms computed from the vector magnetometer measurements as shown in (9).

$$\cos X = \frac{B_x}{B_t}, \qquad \cos Y = \frac{B_y}{B_t}, \qquad \cos Z = \frac{B_z}{B_t}, \tag{9}$$

where B_x, B_y, and B_z are the vector measurement components.

Improved Aircraft Magnetic Compensation

The Tolles-Lawson model presented above is a linear model. It's simplicity works well for the small disturbance fields seen in geo-survey aircraft. On aircraft with larger disturbance fields and disturbances from aircraft systems and electronics, this model alone will be unable to compensate for the aircraft disturbance field well enough to allow for magnetic navigation. The development of non-linear models or the use of machine learning algorithms show promise moving forward for improving compensation [21]. Machine learning in particular could determine the relationship between a collection of known magnetic anomaly values and a collection of model input parameters, such as the vector magnetometer measurements. Additional model input parameters could be added for aircraft systems, such as engine rotation or control surface deflections. This would require flight over a magnetic anomaly map with a known position to be able to collect known magnetic anomaly values.

2.2 Aerial Vision-Aided Navigation

Aerial vision-aided navigation uses computer vision algorithms to match features between aerial imagery and a database of reference imagery. An estimate of aircraft position is extracted from matching image features and the position is used to aid aircraft inertial measurements. Reference imagery is available for a large portion of the Earth through the use of satellite imagery, but it is not available world-wide or at all times. A significant disadvantage of vision navigation systems are their limitations over large areas of feature-less terrain, such as oceans, forests, and deserts. Weather, such as clouds or snow-covered terrain, can also significantly impact some forms of vision navigation. Another disadvantage to vision navigation systems is the computing power required for computer vision algorithms to operate in real-time with a database of reference imagery. If the algorithm must search over a large number of

reference images to cover a large area of potential matching features, then it will not be able to compute a solution in real-time. However, vision navigation systems have shown much promise in achieving GPS-level accuracy. Venable's work in [2] presents a vision-aided navigation system that fuses aerial information from aerial imagery with information extracted from satellite imagery to estimate a position reportable to an INS. Their algorithm is able to recover a coarse position and bootstrap a fine-tracking algorithm to provide position estimates to a tactical grade INS. With real flight data, they were able to demonstrate horizontal position accuracies better than 5 meters on a 45 minute flight [2].

This research employs a "black box" vision-aided navigation solution that follows the work done by Venable in [2]. The following subsections will provide the reader with a limited background on computer vision and how it pertains to the vision-aided navigation system within this research.

2.2.1 Camera Modeling and Calibration

The basic computer vision system relies on a perspective projection model, which allows for the mapping from the 3-D world to a 2-D image plane. Perspective projection assumes a pinhole camera model where the image is formed by the intersection of light rays through the optical center of the camera with the 2-D image plane [26]. A depiction of perspective projection is shown in Figure 9. The mapping from the 3-D world to the 2-D image plane is given by the perspective projection equation

$$\lambda \begin{bmatrix} u \\ v \\ 1 \end{bmatrix} = \mathbf{K} \begin{bmatrix} X \\ Y \\ Z \end{bmatrix} = \begin{bmatrix} f_x & 0 & u_0 \\ 0 & f_y & v_0 \\ 0 & 0 & 1 \end{bmatrix} \begin{bmatrix} X \\ Y \\ Z \end{bmatrix}, \tag{10}$$

where λ is the depth factor, $\mathbf{K}$ is the camera calibration matrix, f_x and f_y are the

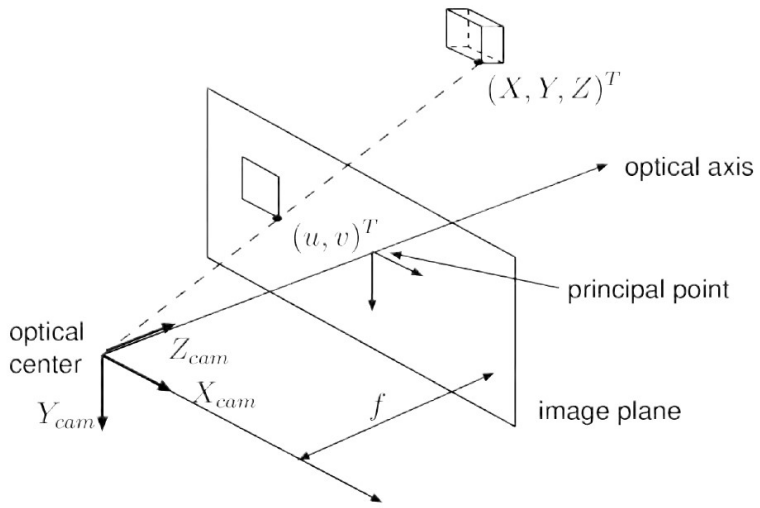

Figure 9: Perspective projection model. Mapping a 3-D object onto a 2-D image plane [27].

focal lengths, and u_0 and v_0 are the principal point coordinates on the image plane. These parameters are computed during camera calibration [26].

A pinhole camera model assumes there are no lenses used to focus light, and that there is a perfect projection of the 3-D world onto the image plane. The addition of lenses introduces radial distortion into the projection. This distortion can be modeled using a higher order polynomial and applied to the object coordinates to create a set of distorted coordinates. The coefficients of this polynomial, known as distortion parameters, are computed during camera calibration [26].

Camera calibration is the measurement of both intrinsic and extrinsic parameters of the camera system. Intrinsic parameters are those that were discussed above and are related to the camera itself. Extrinsic parameters are the lever arms and orientations relating the camera to the aircraft or navigating vehicle. Intrinsic calibration parameters are computed by taking multiple pictures of an image with distinguishable points of known 2-D geometry, such as a planar checkerboard-like pattern [26].

To expand on the camera model one step further, we will incorporate a world

coordinate frame that gives the camera a position and orientation. The camera has a rotation (R) and translation (t) in relation to the origin of the world coordinate frame, as depicted in Figure 10. Equation (10) can be expanded to

$$\mathbf{x}_p = \mathbf{P}\ \mathbf{X}_w = \mathbf{K}\ [\mathbf{R} \mid \mathbf{t}]\ \mathbf{X}_w, \tag{11}$$

where

$$\mathbf{x}_p = \begin{bmatrix} u \\ v \\ 1 \end{bmatrix}, \qquad \mathbf{X}_w = \begin{bmatrix} X_w \\ Y_w \\ Z_w \\ 1 \end{bmatrix}. \tag{12}$$

The camera matrix, $\mathbf{P}$ describes how the world coordinates (X_w, Y_w, and Z_w) project into the image plane through use of the rotation ($\mathbf{R}$) and translation ($\mathbf{t}$) of the camera, as well as the camera calibration matrix ($\mathbf{K}$) [28].

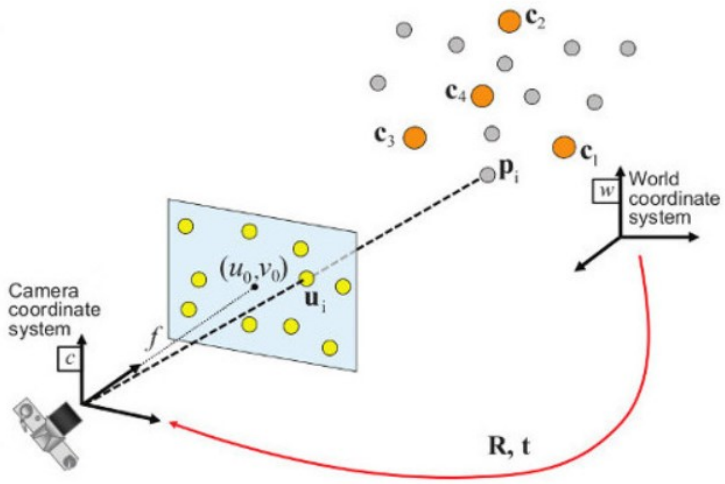

Figure 10: Position and orientation of a camera in a World coordinate frame [29].

2.2.2 Image Features

With computer vision, we want to find matching points between different images of an environment. This allows us to extract information from two related images. Matching points, or image features, are characteristics in an image that are uniquely recognizable [30]. In a navigation system that utilizes computer vision, the most important type of image features are point features such as corners or blobs. Their position in an image can be measured accurately. A corner is a point at the intersection of two or more edges. A blob is an image pattern that differs from its immediate neighborhood in terms of intensity, color, and texture [31]. The ideal point feature appears in multiple images and is unique compared to other features in the same area. Additionally, it would correspond with a stationary object (ideally with known coordinates) or an object with known velocity. Finding and matching these features across multiple images requires a detection of the feature as well as a description of the feature [28].

Feature Detection

A feature detector will find where the features are in the image. A good detector will have localization accuracy, repeatability, computational efficiency, robustness to noise, distinctiveness across images, and invariance to photometric and geometric changes [31]. Common corner detectors are the Harris corner detector [32] and the Shi-Tomasi corner detector [33]. They are computationally efficient but lack distinctiveness across images. Blob detectors on the other hand are more distinctive, making them better suited for vision navigation. However, they are computationally slow compared to corner detectors. Common blob detectors are scale invariant feature transform (SIFT) [34] and speeded up robust features (SURF) [35]. SIFT is widely considered the highest performing feature detector (and feature descriptor),

but comes with a computational cost. It detects features by identifying local maximums or minimums through comparison of different levels of Gaussian blurring [34]. An example of an image with SIFT features is shown in Figure 11.

Feature Description

Feature description consists of computing what the feature "looks like". The region around each detected feature is used to compute a compact descriptor that stores relevant information about the feature. This descriptor is used to match features across multiple images [31]. An ideal descriptor will be invariant to scale, rotation, and viewing angle. The simplest type of descriptor is appearance—the intensity of the pixels around a feature. However, the appearance usually changes with scale, rotation, and viewing angle so it is not a good descriptor of information for matching across multiple images. SIFT and SURF are again two of the more popular descriptors for point features. SIFT decomposes the area around a feature into a histogram of gradient orientations. This method has proved to be stable against changes in scale, rotation, and viewing angle [31]. SURF was created with the desire to have something more computationally efficient than SIFT. Details on SURF can be found

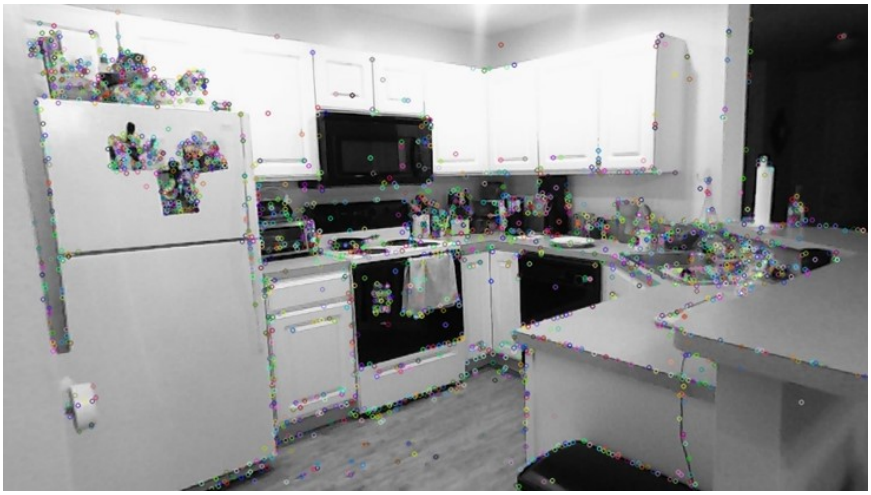

Figure 11: Example image containing SIFT features.

in [35].

Feature detectors and descriptors are not one-size-fits-all solutions. Specific applications and environments require different algorithms. For example, a corner detector might be better-suited in an urban environment with many buildings and corners than a blob detector [31]. Computational efficiency is also large factor. There are many algorithms that exist beyond SIFT and SURF that look to improve on computation times; however, they are beyond the scope of this research.

Feature Matching

The goal of feature detection and description is largely the same for most applications, increase the probability of feature matching between images of the same scene. Feature matching searches for corresponding features between images. To simplify the problem, assume we compare all features in one image to all features in another. Descriptors are compared based on their similarity, and if they are high enough in similarity then they are considered a match [31]. Feature matches between two images are shown in Figure 12.

Outlier rejection methods are used to identify and remove bad matches (a few are seen in Figure 12. A commonly used robust outlier rejection method is random sample consensus (RANSAC). RANSAC randomly selects a number of points required to fit

Figure 12: Feature matching between two images with orientation change. SIFT was used for both feature detection and description.

a model, fits a model using those points, then tests all other data against the model to record points that fit the model well [36]. With two images containing a good set of matching features, the relative orientation between the two images can be computed using visual odometry [26]. Visual odometry is used with vision navigation systems that rely on relative positioning, where you want to know you position in relation to a previous position of yours. An absolute positioning system, which is used in this research, operates using different methods.

2.2.3 Absolute Positioning with Vision

An absolute positioning vision navigation system provides a set of camera coordinates in a World reference frame similar to how GPS reports latitude, longitude, and altitude. Refer to the last example where we had two images containing a good set of matching features. Now suppose that the first image's features are of known World coordinates. The second image's matched features can now be used to compute the camera's orientation in the World frame.

Perspective-N-Point (PnP) algorithms use detected 2-D keypoint features in an image, and their matched 3-D landmark features to estimate camera rotation and translation [2]. Recall Equation (11),

$$\mathbf{x}_p = \mathbf{P}\ \mathbf{X}_w = \mathbf{K}\ [\mathbf{R} \mid \mathbf{t}]\ \mathbf{X}_w,$$

where

$$\mathbf{x}_p = \begin{bmatrix} u \\ v \\ 1 \end{bmatrix}, \qquad \mathbf{X}_w = \begin{bmatrix} X_w \\ Y_w \\ Z_w \\ 1 \end{bmatrix}.$$

If we consider our measurement $\mathbf{z}$ to be the x and y locations of the observed feature in the image plane, then we can write out the measurement equation as

$$\mathbf{z} = \mathbf{x}_p = h(\mathbf{X}_w, \mathbf{R}, \mathbf{t}, \mathbf{K}, distortion\ parameters) + noise. \tag{13}$$

The classic PnP algorithm would seek to solve for $\mathbf{R}$ and $\mathbf{t}$ using

$$\arg\min_{\mathbf{R},\mathbf{t}} \|\mathbf{z} - h(\mathbf{X}_w, \mathbf{R}, \mathbf{t}, \mathbf{K}, distortion\ parameters) + noise\|^2. \tag{14}$$

Equations were obtained from [28] and derived from a full discussion on PnP algorithms in [37]. An illustration of the PnP problem in an airborne environment for vision-aided navigation is shown in Figure 13.

A reference collection of aerial or satellite images serves as the landmark database.

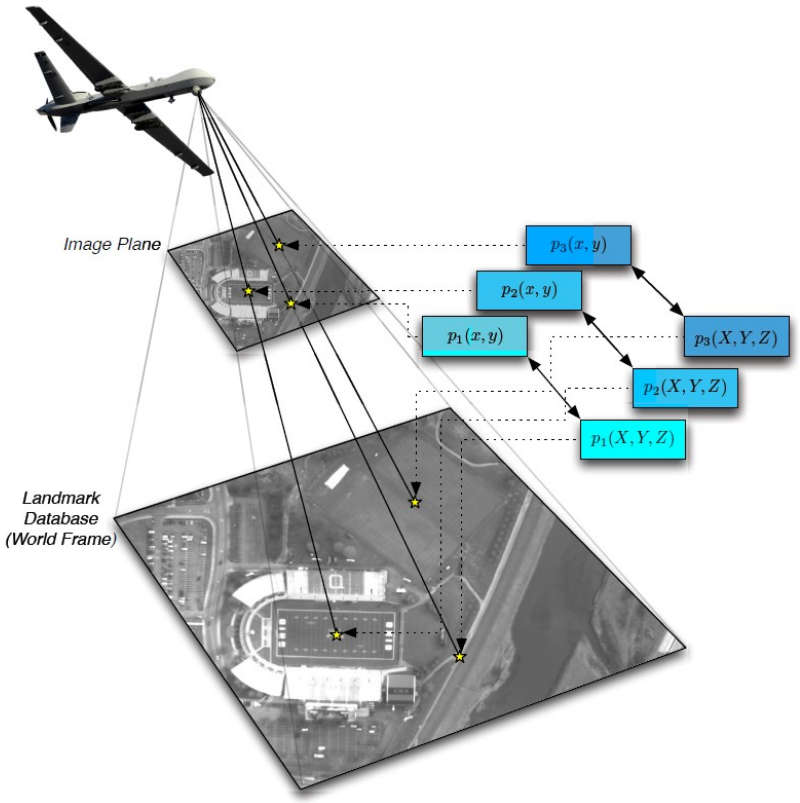

Figure 13: Illustration of the PnP problem while airborne [2].

The landmark database contains high-resolution images that contain image features with known World coordinates, called landmarks. Real-time aerial imagery can then be collected and matched to the landmark database to estimate position. Since computer vision algorithms are generally computationally expensive, the vision-aided navigation system cannot search the entire landmark database in real-time to find a matching image. Using a previous estimate of position, the vision-aided navigation system can search within a limited area for a matching image. The larger the uncertainty around the previous position, the more challenging this task becomes. Course positioning algorithms exist for vision-aided navigation [2], but another navigation system—such as magnetic navigation—can also be used to serve that purpose.

2.3 Extended Kalman Filter

The extended Kalman filter (EKF) is the traditional estimation method used for applications with non-linear dynamics or non-linear measurement models. It is the standard recursive data processing algorithm that is used in many fielded navigation systems. While it may not be the best solution for either magnetic navigation or vision-aided navigation alone, it is a simple and computationally inexpensive method to apply to a navigation system that utilizes both magnetic and vision measurements. This section provides the basic equations needed to implement an EKF following [38], which should be referenced for the full derivation and further discussion.

Assume system state dynamics and measurement models are governed by non-linear functions f and h, respectively. The non-linear system is expressed as

$$\mathbf{x}_k = f(\mathbf{x}_{k-1}, \mathbf{u}_k) + \mathbf{w}_k, \tag{15}$$

$$\mathbf{z}_k = h(\mathbf{x}_k) + \mathbf{v}_k, \tag{16}$$

where

$\mathbf{x}_k$ is the state vector at discrete time step k

$\mathbf{x}_{k-1}$ is the state vector at the previous time step

$\mathbf{u}_k$ is the input vector at time k

$\mathbf{w}_k$ is the additive white Gaussian noise (AWGN) vector of the state dynamics model, with covariance matrix $\mathbf{Q}$

$\mathbf{z}_k$ is the measurement vector at time k

$\mathbf{v}_k$ is the AWGN vector of the measurement model, with covariance matrix $\mathbf{R}$.

The EKF, similar to the Kalman filter, implements a series of propagation and measurement update steps that estimate the system states at discrete points in time. The state estimates are normally distributed and are defined by an estimated mean vector ($\hat{\mathbf{x}}$) and covariance matrix ($\mathbf{P}$). Time steps are still denoted by a subscript k, where $k-1$ would mean the previous time step. Measurement updates are denoted in superscripts by a minus sign (before measurement update, -) and a plus sign (after measurement update, +).

Linearization and Jacobian Matrices

Firstly, the non-linear functions f and h of the system state dynamics and measurement models must be linearized to form their respective Jacobian matrices, $\mathbf{F}$ and $\mathbf{H}$. The linearization is performed by first order Taylor series expansion. The Jacobian matrices are defined as,

$$\mathbf{F}_k \triangleq \left.\frac{\delta f(\mathbf{x},\mathbf{u})}{\delta x}\right|_{x=\hat{\mathbf{x}}_k^+}, \tag{17}$$

$$\mathbf{H}_k \triangleq \left.\frac{\delta h(\mathbf{x})}{\delta x}\right|_{x=\hat{\mathbf{x}}_k^-}. \tag{18}$$

State Propagation

The propagation step propagates the state mean vector and covariance matrix forward in time. Propagation is performed with

$$\hat{\mathbf{x}}_k^- = f(\hat{\mathbf{x}}_{k-1}^+, \mathbf{u}_k), \tag{19}$$

$$\mathbf{P}_k^- = \mathbf{\Phi}_{k-1}\mathbf{P}_{k-1}^+\mathbf{\Phi}_{k-1}^T + \mathbf{Q}_d, \tag{20}$$

where

$\mathbf{\Phi}$ is the matrix exponential of the state dynamics Jacobian matrix, $\mathbf{F}$

$\mathbf{Q}_d$ is a discretized version of the dynamics model noise covariace matrix, $\mathbf{Q}$.

Measurement Update

The next step is to update the states of the EKF with the measurement. The measurement update is performed with

$$\hat{\mathbf{x}}_k^+ = \hat{\mathbf{x}}_k^- + \mathbf{K}_k[\mathbf{z}_k - h(\hat{\mathbf{x}}_k^-, k], \tag{21}$$

$$\mathbf{P}_k^+ = (\mathbf{I} - \mathbf{K}_k\mathbf{H}_k)\mathbf{P}_k^-, \tag{22}$$

where $\mathbf{I}$ is the identity matrix and $\mathbf{K}$ is the Kalman Gain term defined by

$$\mathbf{K}_k = \mathbf{P}_k^-\mathbf{H}^T[\mathbf{H}\mathbf{P}_k^-\mathbf{H}^T + \mathbf{R}]^{-1}. \tag{23}$$

2.4 15 State Pinson INS Error Model

The complex and non-linear system dynamics of a moving vehicle can be modeled using INS measurements and a linearized INS error state model. A commonly known model of this type is the Pinson error model, fully derived in [39]. 15 states can be

used to model:

- 9 states for errors in position, velocity, and attitude
- 6 states for sensor biases in accelerometers and gyroscopes

The full state vector is

$$\mathbf{x} = \begin{bmatrix} \Delta lat \\ \Delta lon \\ \Delta alt \\ \Delta v_n \\ \Delta v_e \\ \Delta v_d \\ \Delta \epsilon_x \\ \Delta \epsilon_y \\ \Delta \epsilon_z \\ bias_a^x \\ bias_a^y \\ bias_a^z \\ bias_g^x \\ bias_g^y \\ bias_g^z \end{bmatrix} \tag{24}$$

Implementation of the Pinson error model and the equations are covered in depth in [39] and are summarized in [1]. Along with the Pinson error model, inertial measurement unit (IMU) model parameters are also required. These parameters change based on the model and type of IMU being used in the navigation filter. The required parameters follow from [39] and are typically found in the specification sheets for each IMU:

- VRW is velocity random walk. It is the noise strength of the velocity errors in accelerometers, modelled as Brownian motion (random walk).
- ARW is the angular random walk. It is the noise strength of the tilt errors in gyroscopes, modelled as Brownian motion.
- σ_{accel} is the standard deviation of accelerometer error.
- σ_{gyro} is the standard deviation of gyroscope error.
- τ_{accel} is the time constant of accelerometer error. It is used with σ_{accel} to model a FOGM process.
- τ_{gyro} is the time constant of gyroscope error. It is used with σ_{gyro} to model a FOGM process.

2.5 Scorpion Plug-and-Play Navigation Framework

Scorpion was a plug-and-play navigation framework developed by the Autonomy and Navigation Technology (ANT) Center at AFIT. The plug-and-play framework was designed to create modular components for real-time navigation filters. Sensor modules, algorithms, and estimation filters are designed separately and used similar to an "off the shelf" product. Pluggable modules for alternative navigation systems, such as magnetic navigation or vision-aided navigation, can be used together with

existing solutions to INS models and estimation filters [40]. The ANT Center has since moved away from Scorpion to a similarly functioning plug-and-play navigation framework, but the existing Scorpion framework was used for this research.

III. Methodology

This chapter details the two research areas explored in this thesis. First, a simulation is used to demonstrate a navigation filter that combines magnetic and vision-aided navigation. In the simulation, synthetic magnetic field measurements are added to real flight test computer vision (aerial imagery) and inertial measurement unit (IMU) data. The objective is to design a functioning 3-D magnetic navigation module in Scorpion, and demonstrate that a magnetic navigation system can be used to bound a navigation solution and initialize a vision-aided navigation system with real aerial imagery data. The navigation filter is described in Section 3.1. The work implements previous research on the design of an aerial magnetic navigation system [1] and an absolute positioning vision-aided navigation system [2]. Section 3.2 details the creation of the synthetic magnetic field measurements that are used in the simulation. Second, a flight test F-16 magnetic field data set is used to demonstrate magnetic navigation on a dynamic, operational platform that contains large aircraft disturbances. The objective is to use a limited approach to aircraft magnetic compensation, then resolve a navigation solution with the compensation results. A bounded navigation solution on the F-16 would show promise for initializing a theoretical vision-aided navigation system. Section 3.4 discusses the limited methods for aircraft magnetic compensation and magnetic navigation that were conducted. Section 3.6 describes both the flight test computer vision and F-16 magnetic field data sets used for this research.

3.1 Navigation Filter

The Scorpion plug-and-play navigation framework developed at the Air Force Institute of Technology (AFIT) is used to implement both magnetic and vision-aided

navigation systems. A "real-time" navigation solution can be obtained with playback of flight test and synthetic sensor data. A magnetic navigation measurement processor was programmed into Scorpion and an existing vision-aided navigation system is used. The systems are combined with an extended Kalman filter (EKF) to aid an inertial navigation system (INS) for positioning. Existing modules for an EKF and an INS are available in Scorpion. The navigation filter as detailed in the following sections is used for the magnetic and vision-aided navigation simulation research for this thesis. A nearly identical navigation filter, implemented in MATLAB, is used for the F-16 magnetic navigation research and is detailed further in Section 3.4.2.

3.1.1 Filter States

The navigation filter estimates 17 states. The first 15 states are from the 15 state Pinson INS error model described in Section 2.4. They include error states for position, velocity, and attitude and sensor bias states for the IMU. Two additional states are added for the magnetic navigation system. The first is a constant bias state to estimate a constant scalar magnetic intensity bias inherent to the compensation process for the aircraft disturbance field and space weather effects. The second additional state is a first-order Gauss Markov (FOGM) state to estimate low-frequency variations in the scalar magnetic intensity from space weather effects and additional unmodelled errors [1]. The complete state vector for the navigation filter is

$$\mathbf{x} = \Big[\Delta lat \;\; \Delta lon \;\; \Delta alt \;\; \Delta v_n \;\; \Delta v_e \;\; \Delta v_d \;\; \Delta \epsilon_x \;\; \Delta \epsilon_y \;\; \Delta \epsilon_z \;\; bias_a^x \;\; bias_a^y \;\; bias_a^z \;\; bias_g^x \;\; bias_g^y \;\; bias_g^z \;\; bias_{mag} \;\; FOGM_{mag}\Big]^T. \tag{25}$$

3.1.2 System Dynamics

The dynamics of the system are modeled using INS measurements and a linearized INS error model, the 15 state Pinson error model described in Section 2.4. This dynamics model is an existing module in Scorpion that is implemented into the navigation filter.

3.1.3 Magnetic Navigation Measurement Module

The magnetic navigation measurement module was programmed into Scorpion for this research. The module implements a measurement model for scalar magnetic intensity measurements to refine the state estimates for latitude and longitude position error. The measurement model presented by Canciani in [1] is expanded to incorporate all known components in the scalar magnetic intensity measurement, as described in Section 2.1.4. In addition to scalar magnetic intensity measurements, the model requires vector magnetometer measurements for aircraft disturbance field removal.

Consider the equation for scalar magnetic intensity measurements in a flight environment

$$z_t = B_{total} = B_{anomaly} + B_{main} + B_{dist} + B_{swe} + v, \tag{26}$$

which includes each of the four components discussed earlier and additive white Gaussian noise (AWGN) v with variance σ^2_{mag}. $B_{anomaly}$ is the anomaly field component, B_{main} is the Earth's main field, B_{dist} is the aircraft disturbance field, and B_{swe} is the field contributed by space weather effects.

The anomaly field is given by

$$B_{anomaly} = M_3(lat, lon, alt), \tag{27}$$

where M_3 is a 3-D gridded linear interpolation function which returns expected magnetic anomaly at a given latitude, longitude, and altitude. The 3-D grid is created from a layered set of upward continuations of a 2-D magnetic anomaly map.

The Earth's main field is computed by

$$B_{main} = WMM(lat, lon, alt, time), \tag{28}$$

where WMM is the World Magnetic Model (WMM), a function of position and time.

The aircraft disturbance field is computed using the Tolles-Lawson compensation model detailed in Section 2.1.5 and is given by

$$B_{dist} = TL(B_x, B_y, B_z, \mathbf{x}_{TL}) + bias, \tag{29}$$

where TL is the Tolles-Lawson model. It is a function of the vector magnetometer measurements (B_x,B_y, and B_z) and the 18 Tolles-Lawson calibration coefficients comprising $\mathbf{x}_{TL}$. There is a constant bias remaining after compensation, which is inherent to sensor calibration of the vector magnetometers themselves [1].

The last component of the measurement equation is from space weather effects, given by

$$B_{swe} = FOGM + bias, \tag{30}$$

were $FOGM$ is a FOGM process. There is a constant bias in addition to the FOGM process.

We can now expand out the measurement equation to arrive at the estimated measurement

$$\begin{aligned} z_t =& M_3(lat, lon, alt) + WMM(lat, lon, alt, time) \\ &+ TL(B_x, B_y, B_z, \mathbf{x}_{TL}) + FOGM + bias, \end{aligned} \tag{31}$$

where both $FOGM$ and $bias$ are system states that are estimated with the 15 state pinson model. The real measurement contains AWGN. The FOGM process is characterized by a standard deviation (σ_{FOGM}) and time constant (τ_{FOGM}), both of which can be optimized in the filter tuning process a discussed in Section 3.5.

Implementation of the measurement equation into the navigation filter results in a non-linear measurement model

$$\mathbf{z}_k = h(\mathbf{x}_k) + TL(B_x, B_y, B_z, \mathbf{x}_{TL}) + \mathbf{v}_k, \tag{32}$$

where

$$\begin{aligned} h(\mathbf{x}_k) =& M_3(lat_{nav} + \Delta lat_k, lon_{nav} + \Delta lon_k, alt_{nav} + \Delta alt_k) \\ &+ WMM(lat_{nav} + \Delta lat_k, lon_{nav} + \Delta lon_k, alt_{nav} + \Delta alt_k, k) \\ &+ bias_{mag,k} + FOGM_{mag,k}. \end{aligned} \tag{33}$$

The Tolles-Lawson model component is separated because it is independent of the filter states. The time step is denoted by k and lat_{nav}, lon_{nav}, and alt_{nav} is the estimated "whole" state reported by the navigation filter. The Jacobian of $h(\mathbf{x}_k)$ is

$$\mathbf{H}_k = \begin{bmatrix} \frac{dh}{d(\Delta lat)} & \frac{dh}{d(\Delta lon)} & \mathbf{0}_{1\times 13} & 1 & 1 \end{bmatrix}, \tag{34}$$

where the derivatives with respect to the Δlat and Δlon states are computed by the central difference method. To simplify notation, combine the M_3 and WMM

functions to a single *mag* function.

$$mag(lat, lon, alt, t) = M_3(lat, lon, alt) + WMM(lat, lon, alt, t), \tag{35}$$

$$\begin{aligned}\frac{dh}{d(\Delta lat)} = \frac{1}{\epsilon}\Big[&mag(lat_{nav} + \Delta lat_k + \frac{\epsilon}{2}, lon_{nav} + \Delta lon_k, alt_{nav} + \Delta alt_k) \\ &-mag(lat_{nav} + \Delta lat_k - \frac{\epsilon}{2}, lon_{nav} + \Delta lon_k, alt_{nav} + \Delta alt_k)\Big],\end{aligned} \tag{36}$$

$$\begin{aligned}\frac{dh}{d(\Delta lon)} = \frac{1}{\epsilon}\Big[&mag(lat_{nav} + \Delta lat_k, lon_{nav} + \Delta lon_k + \frac{\epsilon}{2}, alt_{nav} + \Delta alt_k) \\ &-mag(lat_{nav} + \Delta lat_k, lon_{nav} + \Delta lon_k - \frac{\epsilon}{2}, alt_{nav} + \Delta alt_k)\Big],\end{aligned} \tag{37}$$

where ϵ is equal to one meter converted to degrees latitude or longitude.

Finally, the measurement noise ($\mathbf{v}$) is modeled as AWGN with variance

$$R = E[v^2] = \sigma^2_{mag}, \tag{38}$$

where σ^2_{mag} is the total measurement accuracy. It is not simply the the accuracy of the scalar magnetometer, but also includes white Gaussian noise errors that are present in estimating and removing the aircraft disturbance field and space weather effects [1]. R is another tune-able value to be discussed in Section 3.5.

3.1.4 Vision-Aided Navigation Measurement Module

An existing "black box" vision-aided navigation module was provided by Veth Research Associates to assist with this research. The module uses the navigation

filter's position estimate, aerial imagery, and reference aerial imagery to produce a vision-aided navigation estimate. The navigation filter's covariance is not used in the module, but instead a constant reference imagery search volume is implemented. The "black box" system was developed to support ongoing work with Air Force Research Laboratory (AFRL) for vision navigation research and development. Any results published in this thesis from the vision-aided navigation system are specific to the research in this thesis alone. They should not be used as performance metrics of the specific vision-aided navigation system, but rather the performance of vision-aided navigation systems as a whole. The module expands on the concepts introduced in Section 2.2 and the work completed in [2]. The module runs off of real-time playback of computer-vision imagery. Inputs to the module are the most recent position, velocity, and attitude estimate from the navigation filter, aerial imagery, and a landmark database of aerial imagery. The aerial imagery was from the Ohio Statewide Imagery Program (OSIP), which provides county-wide mosaics of aircraft acquired visual imagery at 1 ft resolution [41]. Additional information on the vision-aided navigation system developed by Veth Research Associates is available to U.S. government agencies and can be requested through AFRL/RYWN [42].

3.1.5 Additional Measurement Functions

Two existing measurement modules are used to simulate Global Positioning System (GPS) and altimeter measurements. The simulated GPS measurements provide updates to the three position error states. They are used to initialize the INS and provide position updates prior to a simulated GPS-outage. The simulated altimeter measurements provide an update to the altitude error state. The magnetic navigation system assumes that altitude updates are provided by another source, so the simulated altimeter measurements are used for the entirety of the flight.

3.2 Synthetic Magnetic Field Measurements

Synthetic magnetic field measurements are generated and combined with flight test computer vision data. The synthetic measurements are generated from the truth position and attitude of the real flight test computer vision data set, discussed further in Section 3.6.1. The main goal of these measurements are to demonstrate the functionality of the magnetic navigation measurement module. They are not intended to be a 100% accurate depiction of what magnetic field measurements would look like. A single set of synthetic vector magnetometer and scalar magnetometer measurements are created for a single flight trajectory's truth position, velocity, and attitude (roll, pitch, and yaw).

3.2.1 Synthetic Vector Magnetometer Measurements

Vector magnetometer measurements are generated to add synthetic aircraft disturbance field to the scalar magnetometer measurements, and so that they can be incorporated into the magnetic navigation measurement module to model the aircraft disturbance field. The synthetic vector measurements are aligned with the aircraft body frame. These measurements are generated using the following process:

1. Compute Earth's main magnetic field vector components at each truth position using the WMM. Both vector and scalar values for the Earth's main field are output as a result of the WMM. Vector components are output in the North, East, and vertical directions for a given latitude, longitude, and altitude. An ideal synthetic vector measurement would incorporate vector components of the magnetic anomaly field in this step (using vector magnetic anomaly maps), but is not conducted for this research.

2. Compute direction cosine matrix (DCM) from North, East, and down (NED)

reference frame to the aircraft body frame using truth attitude. The DCM from the NED frame to the body frame (b) is

$$\mathbf{C}_{NED}^{b} = \begin{bmatrix} 1 & 0 & 0 \\ 0 & \cos\phi & \sin\phi \\ 0 & -\sin\phi & \cos\phi \end{bmatrix} \begin{bmatrix} \cos\theta & 0 & -\sin\theta \\ 0 & 1 & 0 \\ \sin\theta & 0 & \cos\theta \end{bmatrix} \begin{bmatrix} \cos\psi & \sin\psi & 0 \\ -\sin\psi & \cos\psi & 0 \\ 0 & 0 & 1 \end{bmatrix} \tag{39}$$

where ϕ is the aircarft roll angle, θ is the pitch angle, and ψ is the yaw angle.

3. Transform North, East, and vertical (down) components of the Earth's main field to the aircraft body frame. The transformation is computed by

$$\begin{bmatrix} B_x \\ B_y \\ B_z \end{bmatrix} = \mathbf{C}_{NED}^{b} \begin{bmatrix} B_{main,N} \\ B_{main,E} \\ B_{main,D} \end{bmatrix} \tag{40}$$

   From the NED frame to the body frame, the Euler angles are applied in the order yaw, pitch, then roll as depicted in (39) and (40).

4. Add white Gaussian noise to the vector measurement components. The variance used for the simulated measurements was 100^2 nano-Teslas (nT), approximately that of accuracies seen in vector magnetometers.

The resulting synthetic vector magnetometer measurements are shown in Figure 14.

3.2.2 Synthetic Scalar Magnetometer Measurements

To demonstrate the functionality of the magnetic navigation measurement module, synthetic scalar magnetometer measurements must incorporate each of the four

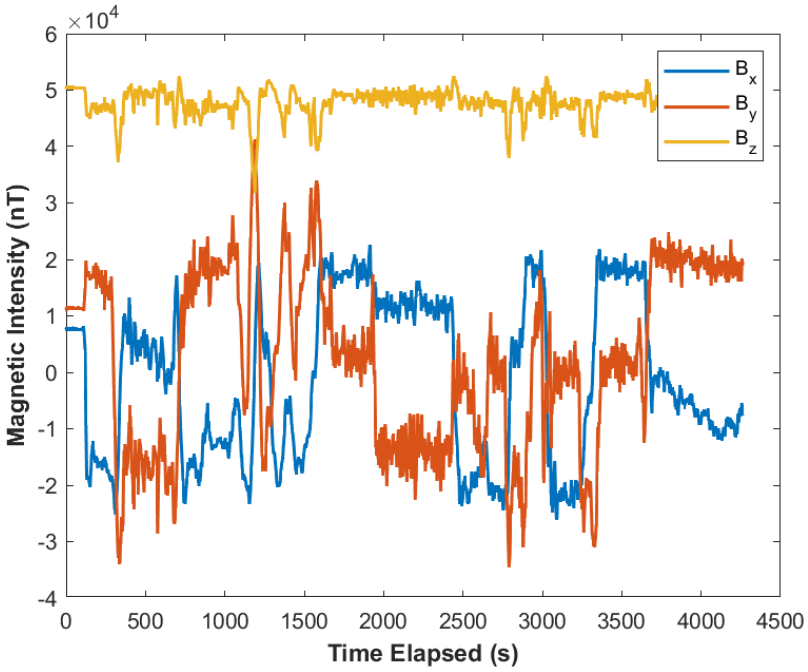

Figure 14: Synthetic vector magnetometer measurements.

components of the scalar magnetic intensity in a flight environment. The synthetic scalar measurement equation is nearly identical to Equation (26) where the only exception is with how the space weather effects are generated. The synthetic scalar magnetic intensity measurement is shown in Figure 15.

$$z_t = B_{total} = B_{anomaly} + B_{main} + B_{dist} + B_{swe} + bias + v \tag{41}$$

Anomaly and Main Fields

The synthetic anomaly field and main field are generated for each truth position on the trajectory. The North American Magnetic Anomaly Database (NAMAD) is used as the magnetic anomaly map for the synthetic measurements. The anomaly field is only generated when the anomaly map exists below the aircraft altitude due to the upward continuation of the map.

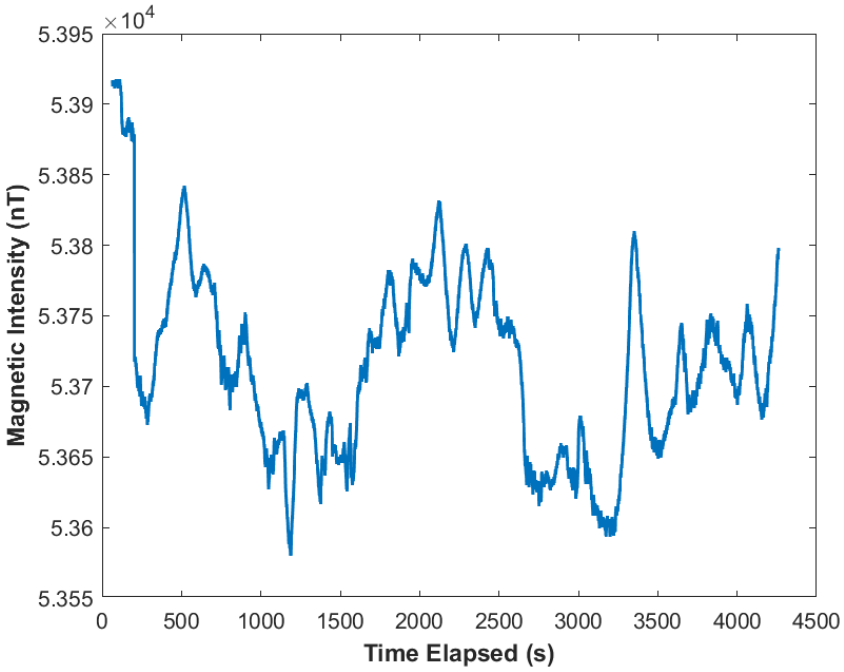

Figure 15: Synthetic scalar magnetometer measurement.

$$B_{anomaly} = M_3(lat, lon, alt), \tag{42}$$

$$B_{main} = WMM(lat, lon, alt, time), \tag{43}$$

The anomaly and main field components of the synthetic scalar magnetic intensity measurement are shown in Figure 16.

Disturbance Field

The aircraft disturbance field is generated by using the synthetic vector magnetometer measurements (without measurement noise) and the Tolles-Lawson compensation model. The 18 calibration coefficients used are

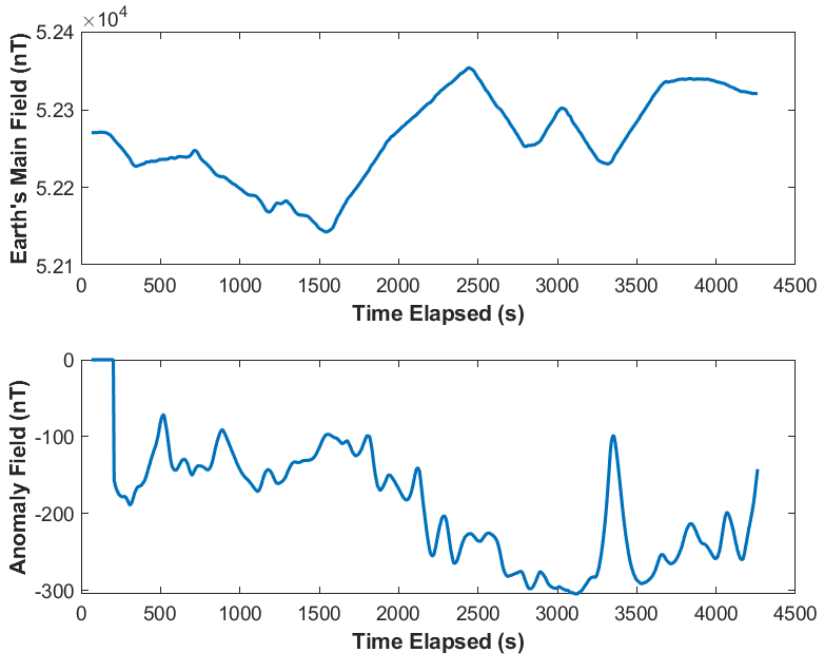

Figure 16: Main and anomaly field components of the synthetic scalar magnetometer measurement.

$$\mathbf{x}_{TL} = \Big[22.04 \;\; -65.87 \;\; 68.20 \;\; 24.81 \;\; 10.43 \;\; 3.74 \;\; -42.68 \;\; -1.92 \;\; -37.46 \;\; 153.19 \;\; -0.67 \;\; 2.17 \;\; -0.91 \;\; 155.27 \;\; -4.43 \;\; 9.85 \;\; 8.37 \;\; 109.81\Big]^T. \tag{44}$$

The coefficients started with calibration coefficients from a geo-survey aircraft. To make the field more visually observable, they are scaled to increase the aircraft disturbance field. The permanent field component is scaled to be approximately three times the magnitude of the induced field component. The total aircraft disturbance field component of the scalar magnetic intensity measurement is shown in Figure 17. The components are separated and shown in Figure 18.

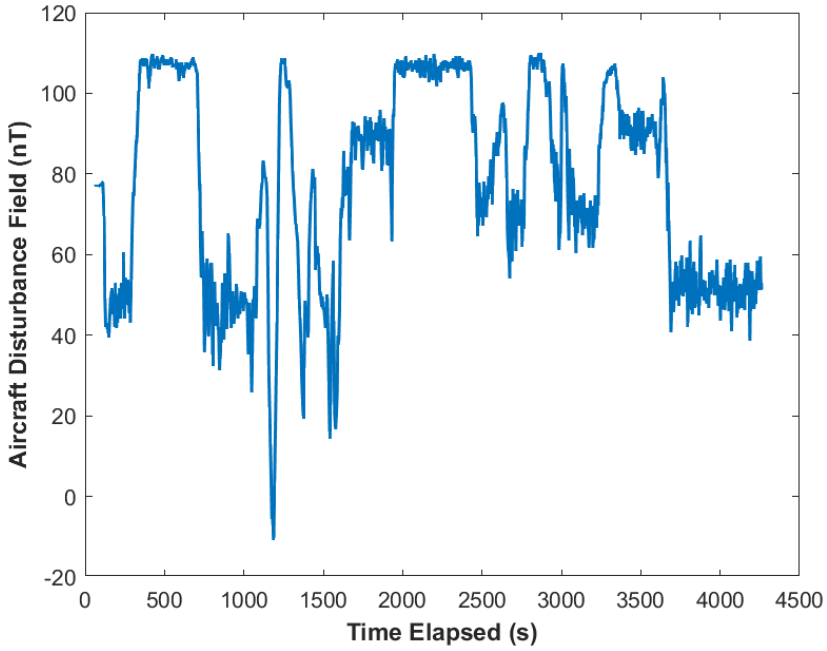

Figure 17: Total aircraft disturbance field component of the synthetic scalar magnetometer measurement.

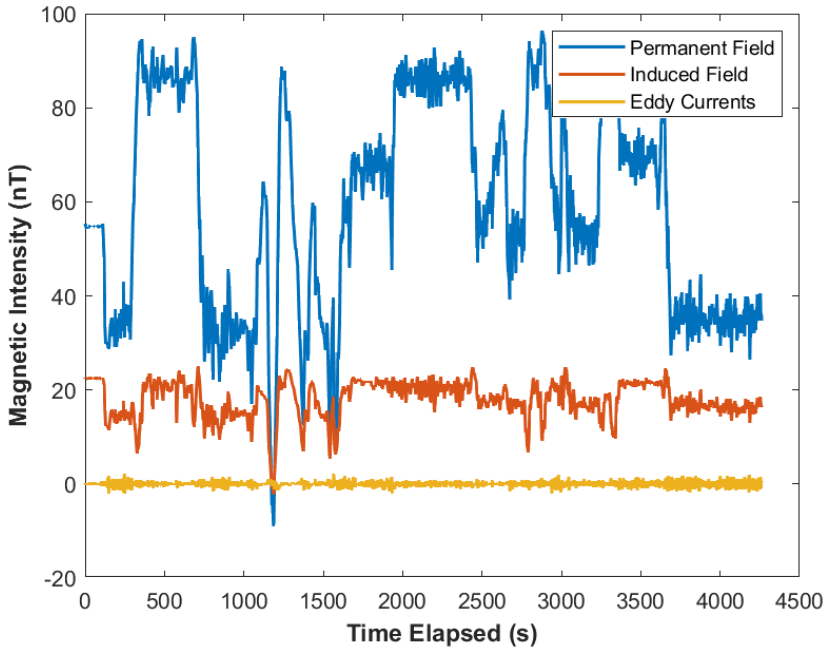

Figure 18: Components of the aircraft disturbance field in the synthetic scalar magnetometer measurement.

Space Weather Effects

The space weather effects are generated by adding magnetic base station data, which geo-survey aircraft usually use to remove the space weather effects post-flight. The base station data is not chosen for the current flight time of the test data, but is a random sample from a collection of data from the same month (June 2019). This sample is chosen as part of a larger effort for generating simulated measurements, and is just meant to be representative of what the space weather effect data could look like at a random time. Base station data is obtained from a base station in Fredericksburg, Virginia [15]. The space weather effect data in the synthetic scalar magnetic intensity measurement is shown in Figure 19.

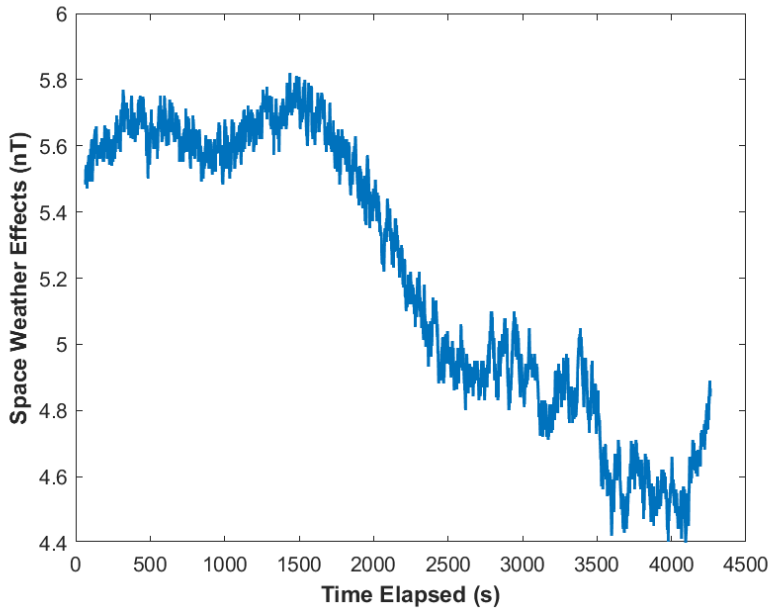

Figure 19: Space weather effects component of the synthetic scalar magnetometer measurement.

Measurement Bias and Noise

A constant bias and white Gaussian noise are added to the measurement. The bias is a randomly generated constant term from zero to 1000 nT, arbitrarily chosen to test functionality of the bias term in the navigation filter. In an ideal synthetic measurement, the bias could also be a negative value. The white Gaussian noise added to the measurement has a variance of 1 nT, the accuracy of a scalar magnetometer. In an ideal synthetic measurement for scalar magnetometers, there would be more noise in the system since 1 nT is not an accurate reflection of the total accuracies seen in the the scalar magnetic intensity measurement in a flight environment [1]. This is ignored to simplify the synthetic measurement for this research.

3.3 Summary of Simulation Methodology

The simulation is used to demonstrate a navigation filter that combines magnetic and vision-aided navigation. Real flight test aerial imagery and IMU measurements are combined with synthetic magnetic field data. The "simulated" aspects are the addition of synthetic magnetic field data, and the conditions of which measurement modules are turned on or off. The objective is to show that magnetic navigation can be used to bound the navigation solution of an aircraft and then initialize a vision-aided navigation system that can obtain higher accuracy positioning estimates. In the next section, the methodology used for demonstrating magnetic navigation on a flight test data set will be discussed. It will be used to show how magnetic navigation can bound the navigation solution on real magnetic field data obtained on a dynamic platform with large magnetic disturbance.

3.4 Magnetic Navigation on an F-16

A limited approach to aircraft magnetic compensation is implemented in an attempt to model and removed the large aircraft disturbance field of the F-16 for a portion of each flight profile. The results of the magnetic compensation are then used to generate a navigation solution.

3.4.1 Limited Compensation of F-16 Aircraft Disturbance

As discussed in Section 2.1.5, the Tolles-Lawson model for aircraft magnetic compensation works well for small disturbance fields. It will be unable to compensate for the aircraft disturbance field of the F-16 to a level where a magnetic navigation solution is feasible. Machine learning algorithms are one method showing promise moving forward for improving compensation [21]. A limited machine learning approach with MATLAB's *Deep Learning Toolbox* [43] is used to compensate for the F-16's disturbance field. Compensation is not a focus of this research. No optimization or experimentation in compensation techniques are performed.

The same model parameters as the Tolles-Lawson model are used as the inputs to the machine learning algorithm—providing a bridge between the traditional methods and a limited implementation of a machine learning method. The first half of the flight profile is used as the machine learning "training set" for that flight, which is then applied to the second half of the flight profile.

Machine Learning Set-Up

Using MATLAB's *Deep Learning Toolbox* a 1-layer, 5 hidden unit dense neural network is trained using Levenberg-Marquardt backpropagation (the default training algorithm) [43]. The neural network inputs are 18 Tolles-Lawson model parameters: 3 for the permanent field model, 6 for the induced field model, and 9 for the eddy

currents model. The neural network output is the expected scalar intensity of the combined anomaly and main field computed using the truth aircraft position. Figure 20 shows a simplified architecture of the neural network.

Compensation from Raw Measurements

Scalar magnetometer, vector magnetometer, and truth positioning measurements are collected for the duration of each flight profile. The following methodology is used to compute compensation error and to arrive at compensated scalar magnetic intensity—the scalar magnetic intensity with the modeled aircraft disturbance field removed.

1. Trim flight trajectory and measurements: Select only flight data that occurs while the aircraft is flying within the magnetic anomaly map.

2. Down-sample magnetometer measurements: The scalar magnetometer (1000

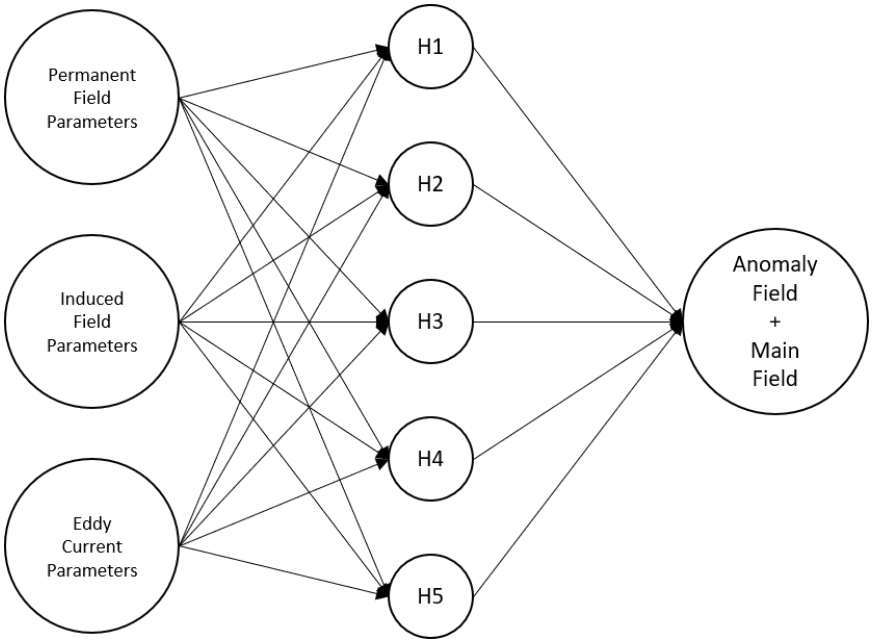

Figure 20: Simplified architecture of F-16 compensation neural network. The 18 Tolles-Lawson input parameters were simplified into the 3 groups shown.

Hz) and vector magnetometer (75 Hz) measurements are down-sampled to 10 Hz. Any navigation signal frequency is expected to be around 1 Hz or less [1]. The measurements are first low-pass filtered to remove any frequency content above 10 Hz to prevent aliasing. A non-causal filter is used so that phase content in the signal is unchanged.

3. Interpolate data onto similar time steps: Interpolate the vector magnetometer and truth positioning measurements onto the same the same time steps as the scalar magnetometer measurements.

4. Compute neural network output: The expected scalar intensity of the combined anomaly and main field are computed using the truth aircraft position.

$$nn_{out} = \Big[M_3(lat, lon, alt) + WMM(lat, lon, alt, time) \Big]_{1 \times N} \tag{45}$$

   There are some flight profiles that are flown at the same altitude of the anomaly map. Altitude was maintained to within approximately 50 m of the map altitude. A constant altitude equal to the map altitude is assumed for these profiles.

5. Compute neural network input: The Tolles-Lawson model parameters are com-

puted using the same methods as discussed in Section 2.1.5.

$$nn_{in} = \begin{bmatrix} \cos X \\ \cos Y \\ \cos Z \\ 1 \\ \cos X \cos Y \\ \cos X \cos Z \\ \cos^2 Y \\ \cos Y \cos Z \\ \cos^2 X \\ \cos X \cos \dot{X} \\ \cos X \cos \dot{Y} \\ \cos X \cos \dot{Z} \\ \cos Y \cos \dot{X} \\ \cos Y \cos \dot{Y} \\ \cos Y \cos \dot{Z} \\ \cos Z \cos \dot{X} \\ \cos Z \cos \dot{Y} \\ \cos Z \cos \dot{Z} \end{bmatrix}_{18 \times N}$$

6. Train neural network: Use data from the first half of the flight profile to train the neural network. The resultant neural network models the expected combined anomaly and main field for the duration of the profile based on Tolles-Lawson input parameters.

7. Run neural network: Run the neural network on the second half of the flight profile. This results in nn_{pred}—a predicted value of the combined anomaly and

main field based on the neural network model and the input parameters. This value is also the compensated scalar magnetic intensity.

8. Compute compensation error: The compensation error is the difference between the expected values for combined anomaly and main field and the predicted values. This allows us to see how effective the compensation was for the duration of the second half of the profile.

$$Error_{comp} = M_3(lat, lon, alt) + WMM(lat, lon, alt, time) - nn_{pred} \quad (46)$$

3.4.2 Navigation Methodology

A MATLAB implementation of the navigation filter discussed in Section 3.1 is used to resolve a navigation solution for one of the F-16 flight profiles, based on compensation results. Since the first half of the flight profile is used to train the machine learning algorithm used in compensation, the second half of the profile is used to apply the machine learning algorithm and test the navigation filter. A few simplifications are made to how the navigation solution is resolved for the F-16 in the MATLAB implementation:

1. Pre-processed scalar measurements: The scalar magnetometer measurements are pre-processed to compensate for the aircraft disturbance field. The pre-processed scalar measurement input for the navigation filter is nn_{pred}.

2. Synthetic IMU measurements: To guarantee that the INS model used in the navigation filter matches any input IMU measurements, synthetic measurements are generated based on the truth positioning measurements. Both tactical grade and navigation grade IMU measurements are generated. Table 2 summarizes the IMU model parameters.

Table 2: Summary of IMU models used to generate synthetic IMU measurements for F-16 magnetic navigation.

	Tactical Grade	**Navigation Grade**
VRW $(\frac{m}{s^2}\frac{1}{\sqrt{Hz}})$	0.3	0.000238
ARW $(\frac{rad}{s}\frac{1}{\sqrt{Hz}})$	6.0602×10^{-7}	5.810×10^{-7}
$\sigma_{accel}(\frac{m}{s^2})$	0.0005	0.000245
$\sigma_{gyro}(\frac{rad}{s})$	7.2722×10^{-7}	7.2700×10^{-9}
$\tau_{accel}(s)$	3600	3600
$\tau_{gyro}(s)$	3600	3600

3.5 Filter Tuning

Both instances of magnetic navigation in this research, simulation on synthetic data and F-16 magnetic navigation, require filter tuning to ensure well-behaved navigation filter output and optimized performance. First, filter tuning is performed to model the FOGM state in the navigation filter. The standard deviation (σ_{FOGM}) and time constant (τ_{FOGM}) of the FOGM are tuned to ensure that the space weather effects and other modelling errors in the navigation solution can be estimated by the FOGM state. For the simulation, values for σ_{FOGM} and τ_{FOGM} are pulled directly from the work done by Canciani in [1]. Canciani analyzed a year's worth of temporal variation data resulting in a σ_{FOGM} of 10 nT and a τ_{FOGM} of 140 minutes. This should be satisfactory for the synthetic magnetic field data since the space weather effects are added to the synthetic measurement using a random selection of actual temporal variation data.

For F-16 magnetic navigation data, the FOGM model parameters are estimated by observing the compensation error. σ_{FOGM} is estimated by simply taking the standard deviation of the compensation error. The time constant describes how quickly the data de-correlates with itself. By observing the compensation error's auto-correlation, τ_{FOGM} is when the compensation error decreases to 36.8% of it's

starting value. MATLAB's cross-correlation function *xcorr* is used to compute the auto-correlation of the compensation error, and the results are observed as depicted in Figure 21.

Another filter tuning parameter is the variance of measurement noise, R. The navigation filter output is observed both for divergent navigation solutions and for solutions where the error mathematically falls outside of the filter estimated standard deviation. If a navigation solution diverges, R can be increased to tune the filter until divergences are eliminated or reduced. R can also be adjusted to optimize the filter estimated standard deviation.

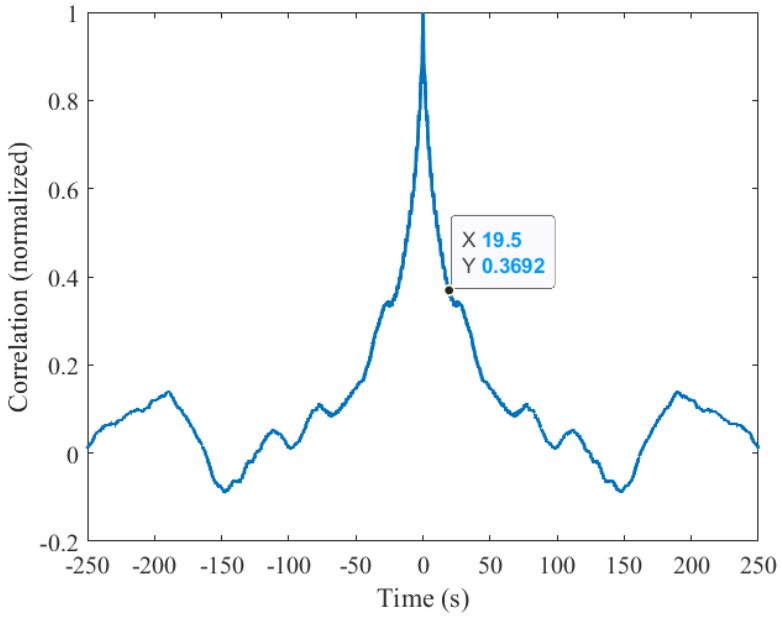

Figure 21: F-16 Profile 1: Auto-correlation of compensation error computed for the second half of profile 1 using a limited machine learning approach to compensation. The time constant is when the compensation error decreases to 36.8% of it's starting value.

3.6 Vision and Magnetic Data Sets

3.6.1 Computer Vision Data Set

AFRL has been a major contributor to work on vision-based navigation systems. In June 2019, a flight test was conducted by AFRL over Dayton, Ohio as part of the positioning, navigation, and timing (PNT) flight test campaign. The test was conducted on a Douglas DC-3 carrying an AgilePod. The following data is used from the 27 June 2019 test flight:

1. Visible Gray-scale Imagery: Captured at 5 Hz from a Prosilica GT2050 camera.
2. Inertial Measurement Unit: Raw delta velocity and delta rotation measurements from a Honeywell HG1700 IMU.
3. Truth Position, Velocity, and Attitude: GPS-aided INS output of aircraft whole state.

A DC-3 aircraft in the same fight test configuration is shown in Figure 22, the AgilePod is fixed to the underside of the aircraft fuselage. The flight trajectory over Dayton, Ohio is shown in Figure 23.

Figure 22: Douglas DC-3 aircraft carrying AFRL's AgilePod (U.S. Air Force photo/-David Dixon) [44]. The DC-3 with AgilePod was used to collect the computer vision data set.

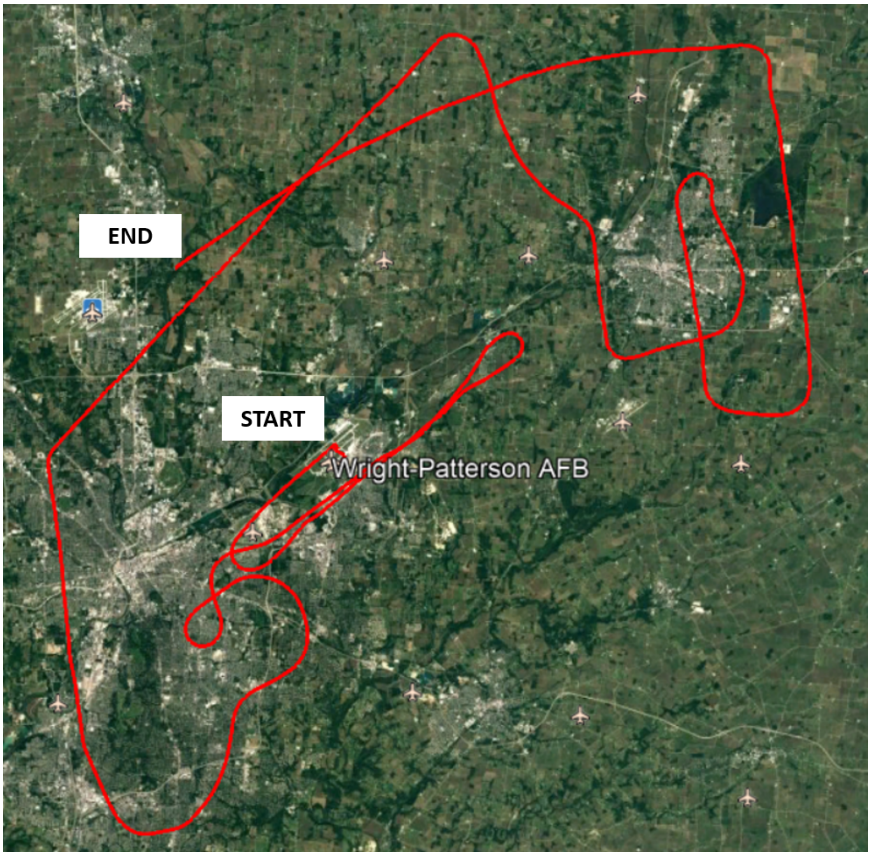

Figure 23: Horizontal position of computer vision data set.

3.6.2 F-16 Magnetic Field Data Set

The U.S. Air Force Test Pilot School (TPS) collected a large magnetic navigation flight test data set in September 2020 [45]. The flight test was conducted over Edwards Air Force Base, California. The test consisted of 17 flights that were flown on an F-16 carrying a RASCAL Pod. The following data is used from nine of the test flights where navigation profiles were flown:

1. Scalar Magnetic Intensity: Collected at 1,000 Hz from a Geometrics MFAM Scalar Magnetometer.

2. Vector Magnetic Field: Collected at 75 Hz from an Applied Physics Systems Model 359 Vector Magnetometer.

3. Truth Position, Velocity, and Attitude: GPS-aided INS output of aircraft whole state. Provided by on-board Time and Space Positioning Information system.

The flight test F-16 is shown in Figure 24 with the RASCAL Pod attached underneath the left wing. More data is available from the F-16 flight testing and is detailed further in [45].

Figure 24: USAF F-16 aicraft carrying TPS's RASCAL pod. The F-16 with RASCAL pod was used to collect the F-16 magnetic field data set.

3.7 Magnetic Anomaly Maps

3.7.1 North American Magnetic Anomaly Database

The NAMAD is used for the simulation demonstrating magnetic and vision-aided navigation. A rectangular portion of the map encompassing the Dayton, Ohio area is used to create the synthetic magnetic field measurements and is also used as a navigation reference. Since it is used for both of these objectives, it can be considered a map of high accuracy. The map altitude is 305 meters above terrain.

3.7.2 High Fidelity Maps at Edwards Air Force Base

High fidelity magnetic anomaly maps are used for the flight test F-16 magnetic field data set. Three magnetic anomaly maps were created by Sander Geophysics Limited over Edwards Air Force Base, California in 2019 [46]. Map details are summarized in Table 3. The maps are shown in Figures 25 through 27.

Table 3: Summary of Edwards Air Force Base magnetic anomaly maps.

Map Name	**Map Altitude (m)**	**Traverse Line Spacing (m)**	**Control Line Spacing (m)**
Cords Road	1066	300	3000
Medium Altitude	2134	1200	6000
Cap Altitude	5334	4800	12000

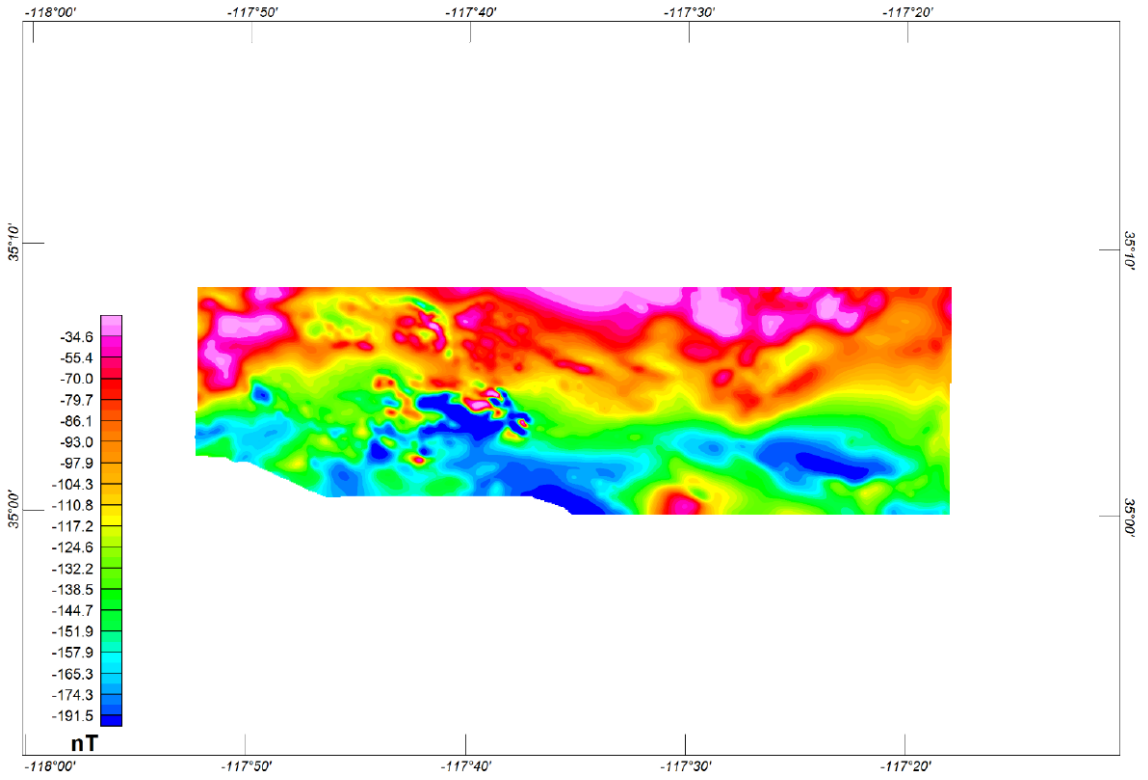

Figure 25: Edwards AFB Flights: Cords Road anomaly map, 1066 meters altitude mean sea level [46].

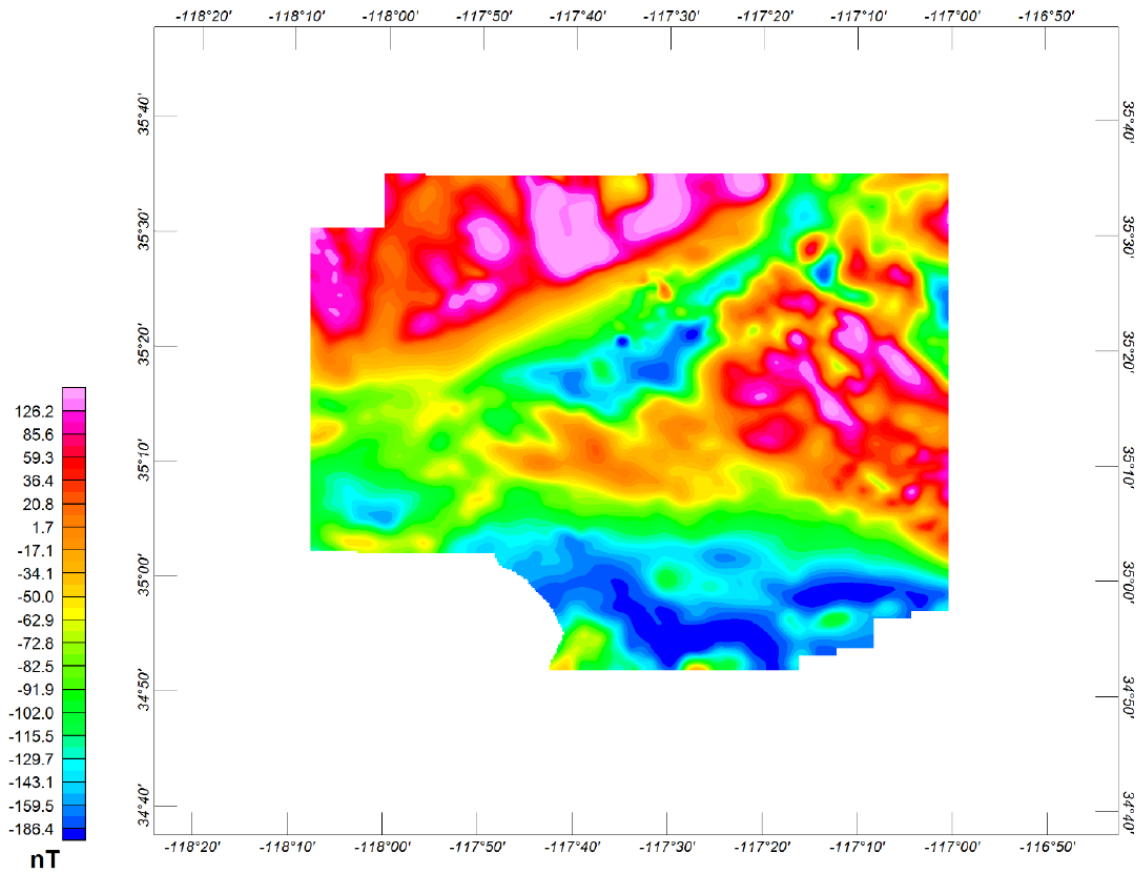

Figure 26: Edwards AFB Flights: Medium Altitude anomaly map, 2134 meters altitude mean sea level [46].

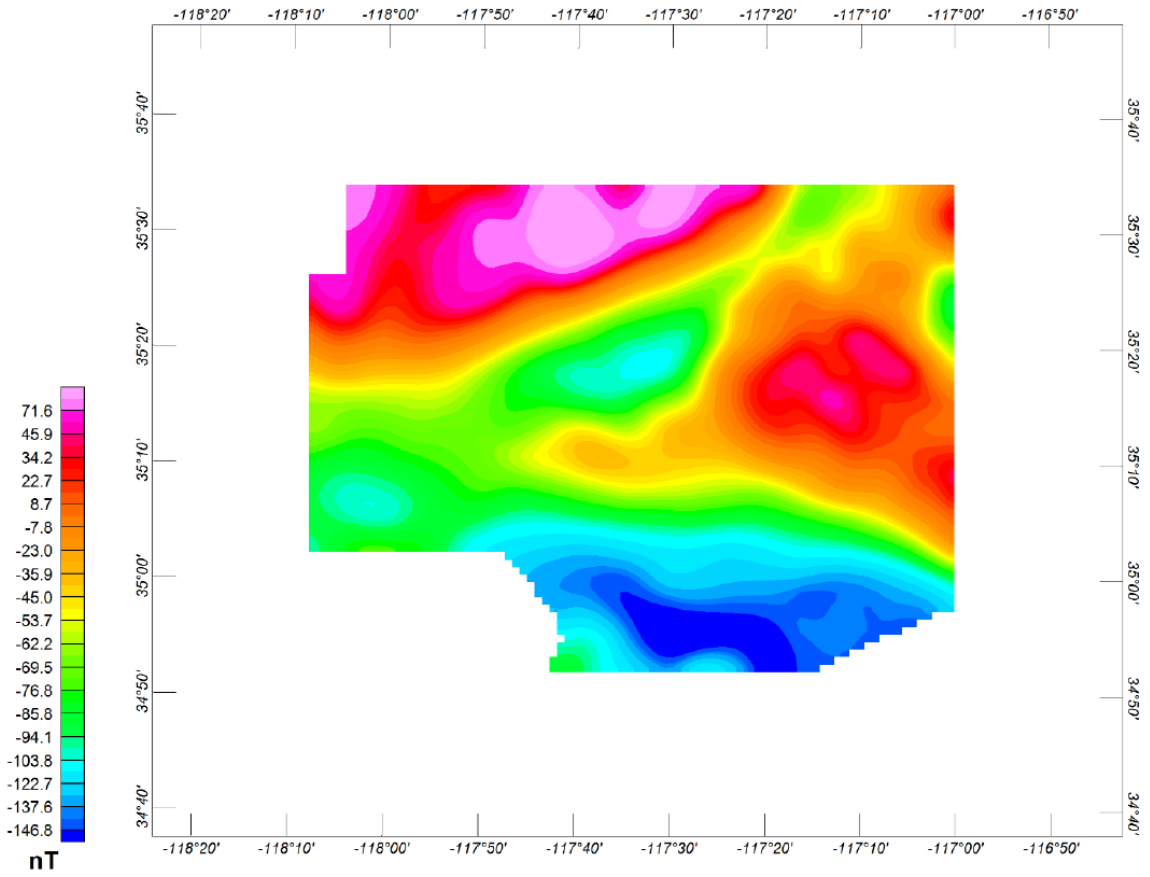

Figure 27: Edwards AFB Flights: Cap Altitude anomaly map, 5334 meters altitude mean sea level [46].

IV. Results and Analysis

This chapter presents the results and analysis of the two research areas in this thesis. First, the simulation results demonstrating magnetic and vision-aided navigation are presented and discussed. The simulations contain real flight test computer vision and inertial measurement unit (IMU) data with the addition of synthetic magnetic field data. Section 4.1 details the simulation cases that were investigated and Section 4.2 provides detailed results and analysis of those cases. Second, magnetic navigation on a dynamic platform is presented using F-16 flight test data. Section 4.4 highlights the flight profiles that were studied. Section 4.5 discusses the aircraft disturbance field observed and the result of limited magnetic compensation for those profiles. The magnetic navigation performance achieved on those flight profiles is then presented in Section 4.6.

4.1 Simulation Cases

The simulation cases for this research are summarized in Table 4. Real flight test computer vision and IMU data are combined with synthetic magnetic field data. The "simulated" aspects are the addition of the synthetic magnetic field data and the conditions of which sensors are turned on and off. A single flight trajectory was used for each case, and sensor contributions to the navigation filter were varied. Simulations include cases with magnetic navigation both on and off. Synthetic magnetic field measurements are used for the magnetic navigation system. Additionally, simulations are configured with vision navigation either observing or aiding the navigation filter. When observing, the vision navigation system is using the current navigation solution to attempt a positioning estimate—it is searching the database of reference imagery based on where the navigation filter estimates the position to be. If a posi-

tioning estimate is successful, a "hit" is reported at that current time step but the estimate is not reported to the navigation filter. When the vision navigation system is aiding the navigation filter, each successful position estimate ("hit") is reported to the filter to aid the navigation solution. Flight test computer vision data from the flight trajectory is used for the vision navigation system and two different computer vision start times are studied.

The single flight trajectory used for all simulation cases is approximately 4,200 seconds in length. It begins on the taxi-way at Wright-Patterson Air Force Base and ends in flight as shown previously in Figure 23 in Section 3.6.1. Global Positioning System (GPS) measurements are used to aid the tactical grade inertial navigation system (INS) for the first 300 seconds of each simulation case. At 300 seconds the GPS measurements are turned off and the remainder of the simulation is performed in the configuration per Table 4. Filter tuning for the magnetic navigation system was conducted as discussed in Section 3.5 and a measurement noise covariance of $R = 4.0$ is used for each case. The vision navigation system was a "black box", it is assumed that it was optimized for performance on this data set.

Table 4: Summary of simulation cases.

Case	**Magnetic Navigation**	**Vision Navigation**	
		Configuration	**Start Time (s)**
1	Off	Observing	300
2	On	Observing	300
3	Off	Aiding	300
4	On	Aiding	300
5	Off	Aiding	1700
6	On	Aiding	1700

4.2 Simulation Results

This section details the results from each of the six simulation cases. The navigation filter horizontal position solutions (North and East Position Error) are plotted for each case to analyze each configuration of the navigation filter. First, simulation cases when the vision navigation system is in the observational configuration are presented—cases 1 and 2. The observational vision navigation system does not report successful position estimates to the navigation filter. Second, in cases 3 and 4, the scenarios are repeated except now the vision navigation system is aiding the navigation filter. Vision "hits" are observed with a vision-aided INS navigation solution, then a magnetic and vision-aided navigation solution. Finally, cases 5 and 6 are presented where the vision navigation system is turned off for an extended period of time after the GPS outage. Case 5 with no magnetic navigation is compared to case 6 with magnetic navigation.

4.2.1 Case 1: INS Only, Vision Observer

Case 1 presents the scenario where a GPS outage occurs with no other alternative navigation source aiding the INS. The vision-navigation system is reporting successful position estimates from real aerial imagery, but it is not aiding the navigation filter. A drifting INS is seen for the entirety of the profile's navigation solution, as seen in Figure 28. Both North and East position error increase unbounded to approximately 20 km by the time the profile is complete, which accurately reflects the unaided drift rate of a tactical grade INS. Vision navigation solution "hits" are displayed as red markers on the x-axis of the plot. At around 700 seconds, the filter error begins to grow and vary more rapidly and there are no successful "hits" beyond that point in the profile. Figure 29 shows a closer look at the first 750 seconds. There are a total of 168 vision "hits" for simulation case 1.

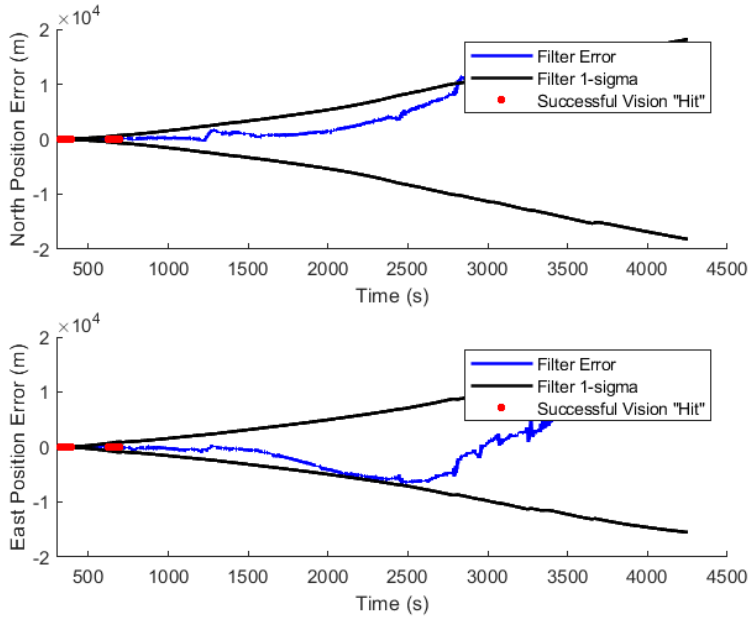

Figure 28: Simulation Case 1 position error results showing INS drift and vision navigation observations ("hits"). There are 168 vision "hits".

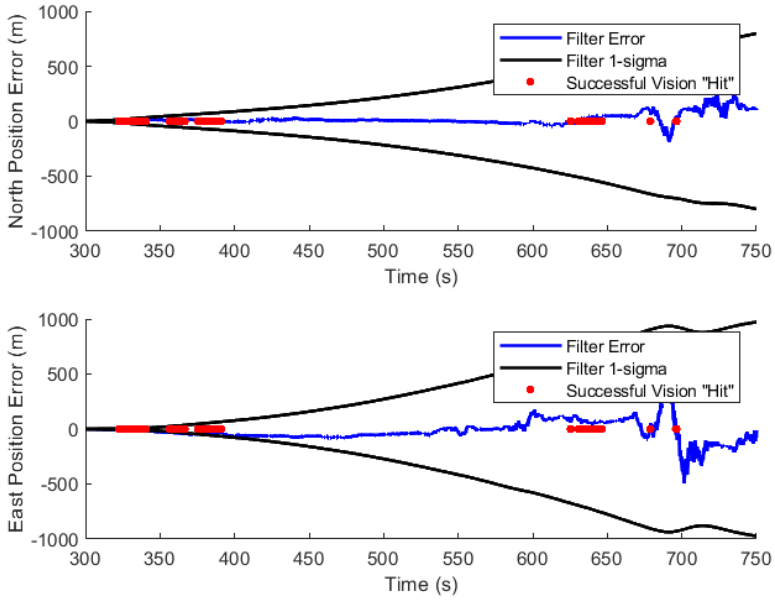

Figure 29: Simulation Case 1 position error results for first 750 seconds, showing all successful vision "hits". There are 168 vision "hits".

4.2.2 Case 2: Magnetic Navigation, Vision Observer

Case 2 simulates magnetic navigation after the same GPS outage seen in Case 1. The vision-navigation system is reporting successful position estimates from real aerial imagery, but it is still not aiding the navigation filter. The magnetic navigation system bounds the drift of the INS, and allows for a course navigation solution for the entirety of the flight profile as seen in Figure 30. This course navigation solution allows for successful vision navigation system "hits" throughout the length of the profile. There are a total of 1,746 vision "hits" for simulation case 2.

There is approximately a 10 times increase in vision "hits" from simulation case 1 to case 2 with the introduction of magnetic navigation in a GPS outage environment. In case 1 we saw that the INS alone will get to a point where an observational vision navigation system is unable to successfully estimate position. It took approximately 700 seconds for that to happen in case 1. In case 2 with magnetic navigation, the observational vision navigation system reported position estimates ("hits") on real aerial imagery for the entirety of the flight profile. Magnetic navigation increases the duration of the flight profile that a vision navigation system can provide "hits". By bounding the INS drift, there is an increased opportunity for success in the vision navigation system. Next, we will observe the same two scenarios again, but with the vision navigation system now aiding the navigation filter.

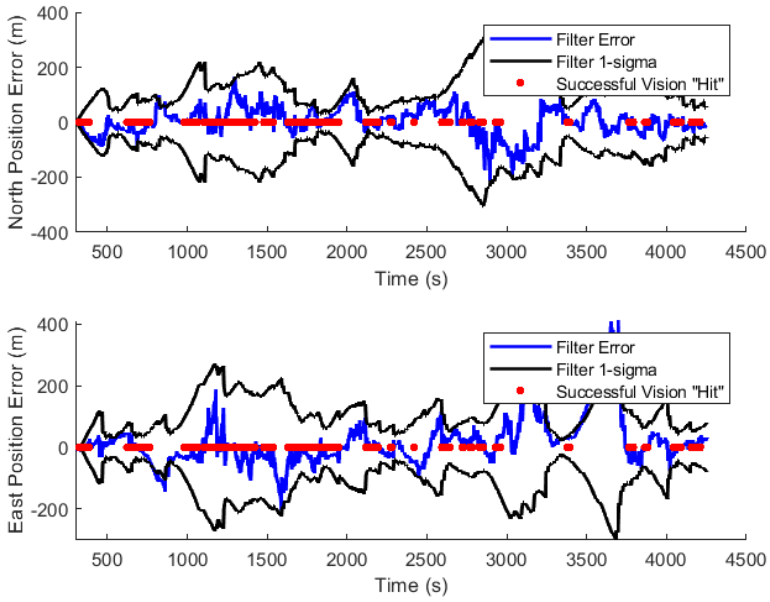

Figure 30: Simulation Case 2 position error results showing magnetic navigation and vision navigation observations ("hits"). There are 1,746 vision "hits".

4.2.3 Case 3: Vision-Aided Navigation

Simulation case 3 studies a vision-aided navigation system after a GPS outage. The vision navigation system is aiding the INS in the navigation filter using real aerial imagery, and magnetic navigation is not present. Figure 31 shows the results of case 3. The vision navigation system successfully provides position estimates to the navigation filter until just under 800 seconds. In those first 800 seconds, there are 316 vision "hits". Figure 32 provides a closer look at the beginning of the profile. There is approximately a 300 second period where there are no vision "hits" and the filter error begins to grow. This is not because there are no images for the navigation system, but there are no successful position estimates provided to the navigation filter. The vision navigation system is able to recover just before 700 seconds and provide a successful position estimate. As expected, the filter error is reduced and more vision "hits" are possible, showing the bootstrapping effect of a navigation filter.

The vision "hits" are short-lived, and after 800 seconds, there are no more successful vision navigation position estimates and the filter error continues to grow unbounded. A position estimate from the vision navigation system is no longer attainable once the error grows too large. This is showing a failure of the vision navigation system and the end results are similar to that of case 1 with the INS only solution. This is an unfortunate effect of a navigation filter that employs only a vision-aided system. If there is a period of time where no useful images are attainable—such as flying through weather or over a body of water—the filter error grows unbounded and if it grows too large a vision solution is impossible. With the addition of another alternative navigation system, such as magnetic navigation, we attempt to bound the growing filter errors enough during vision outages to allow the vision navigation solution to continue providing successful position estimates.

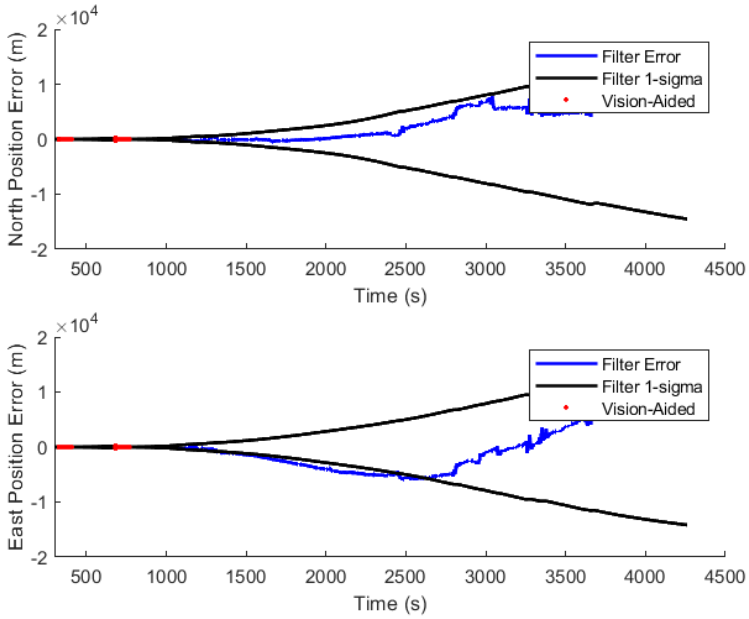

Figure 31: Simulation Case 3 position error results showing vision-aided navigation (no magnetic navigation). There are 316 vision "hits".

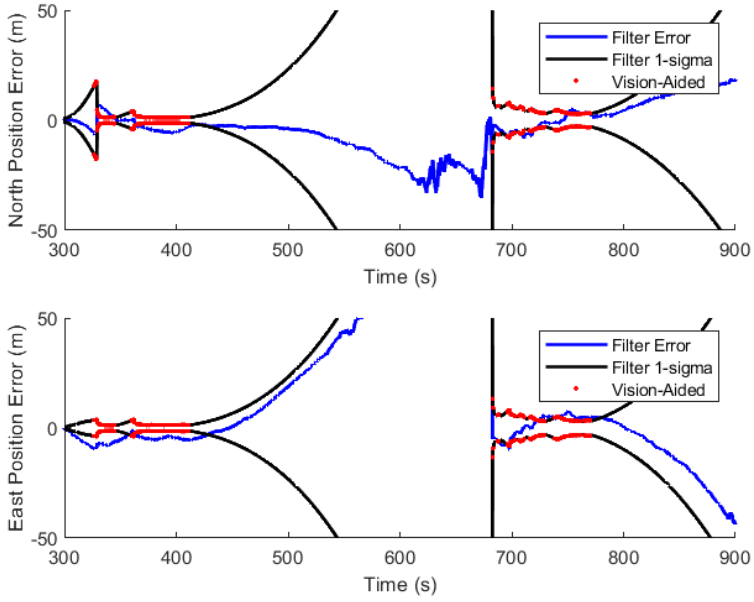

Figure 32: Simulation Case 3 position error results for first 900 seconds, showing all successful vision-aided time. There are 316 vision "hits".

4.2.4 Case 4: Magnetic and Vision-Aided Navigation

Case 4 simulates magnetic and vision-aided navigation after a GPS outage. Both the magnetic navigation and the vision-aided navigation system are aiding the INS in the navigation filter. The navigation results are shown in Figure 33. Similar to case 2, magnetic navigation allows for successful vision "hits" on real aerial imagery throughout the length of the profile. The bootstrapping effect of the vision-aided system is again demonstrated. Now that the vision navigation system is aiding the navigation filter, more "hits" are achieved. There are total of 3,929 vision "hits" for case 4, which is approximately 2.5 times as many as case 2 with the observational only vision navigation system. Unlike the outcome of case 3, magnetic navigation in case 4 prevents large INS drifts during longer vision outages, and allows the vision navigation system to continue providing successful position estimates.

Case 4 is demonstrating a combined magnetic and vision-aided navigation system

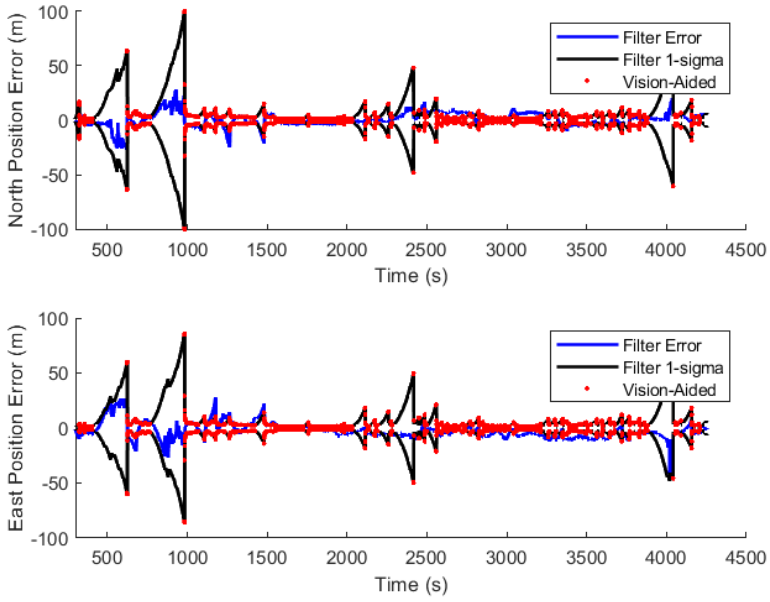

Figure 33: Simulation Case 4 position error results showing magnetic and vision-aided navigation. There are 3,929 vision "hits".

achieving near GPS level accuracy when vision navigation is reporting "hits". A magnetic navigation system—with potential for world-wide availability—can be used with a vision-aided navigation system for a world-wide high accuracy navigation solution. For the duration of simulation case 4, the position errors are under 50 meters in each channel. When the vision navigation system is successfully reporting estimates, position errors are under 10 meters in each channel. The larger position errors are seen during periods when the vision navigation system is unable to provide a successful position estimate. This could during periods of maneuverability, clouds obscuring the ground visibility, or anything else that could effect vision navigation during a flight profile. Magnetic navigation can potentially ensure that vision navigation will always be able to provide a position estimate after periods of long vision outages.

4.2.5 Cases 5 and 6: Navigation After Prolonged Vision-Outage

To further highlight the benefit that magnetic navigation has for a vision-aided system, a longer period of vision outages is observed in simulation cases 5 and 6. Both cases present a scenario where there is a GPS outage at 300 seconds and computer vision data is unavailable for the first 1,700 seconds of the profile. This reflects a potential real-world scenario where the first portion of the profile is flown over a large body of water before making a transition to flight over land. The featureless "terrain" of over-water flight presents one of the largest challenges for a vision-aided navigation system. Case 5 presents the resulting navigation solution of a vision-aided navigation system (no magnetic navigation), and case 6 presents a magnetic and vision-aided navigation system.

Case 5 results are shown in Figure 34. At 1,700 seconds, when the vision navigation system turns on, the system is unable to provide any successful vision "hits" for the remainder of the flight. Since the INS is drifting unbounded for the first 1,700 seconds, the filter errors have simply grown too large before computer vision data becomes available. Adding in magnetic navigation to the filter, case 6 results are shown in Figure 35. The magnetic navigation system bounds the INS drift for the first 1,700 seconds and when the computer vision data becomes available the vision-aided navigation system is able to very quickly provide a position estimate. There are 2,181 vision "hits" once computer vision data is available, compared to zero "hits" when magnetic navigation is not used. In the scenario presented in cases 5 and 6, an only vision-aided system is unable to successfully provide a position estimate from the vision system after a large period of time of no computer vision data, such as in over-water flight. In contrast, a magnetic navigation system is able to bound the INS drift in over-water flight to allow the vision-aided navigation system to achieve successful position estimates once a transition has been made to flying over land.

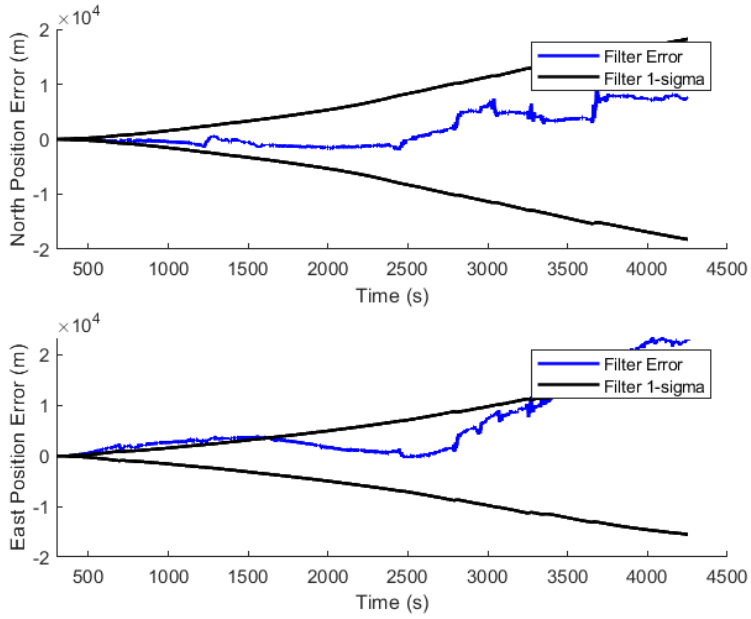

Figure 34: Simulation Case 5 position error results showing INS drift then vision-aided navigation at 1700 seconds. There are zero vision "hits".

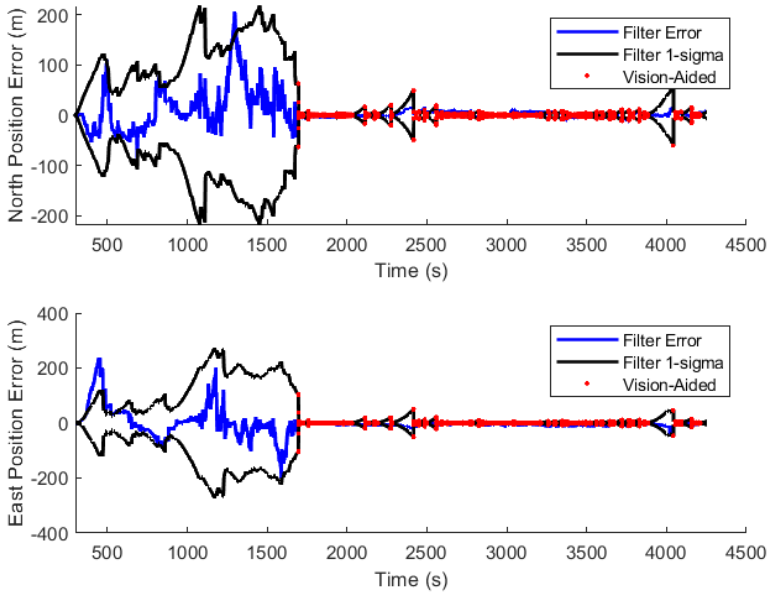

Figure 35: Simulation Case 6 position error results showing magnetic navigation then magnetic and vision-aided navigation at 1700 seconds. There are 2,181 vision "hits".

4.3 Simulation Summary

The results from six simulation cases were presented to demonstrate magnetic and vision aided navigation. Synthetic magnetic field measurements were used along with a real flight test computer vision (aerial imagery) data set. Simulation cases with magnetic navigation both on and off are observed to demonstrate how the vision-aided navigation system is able to perform in each case. The results are summarized in Table 5.

Cases 1 and 2 demonstrate that the addition of magnetic navigation gives an increased opportunity for vision-aided navigation system to successfully estimate position. There is a 10 times increase in vision "hits" in an observational only vision system when the magnetic navigation system is used to bound the INS drift in filter errors. More importantly, the vision navigation system is able to successfully provide position estimates for the entire length of flight, with temporary outage periods. Cases 3 and 4 demonstrate the bootstrapping effect of the vision-aided navigation system and the improvement in results between an only vision-aided system and a magnetic and vision-aided navigation system. The only vision-aided system is able to provide position estimates for the beginning of the flight, but filter errors grow during a vision outage the system is unable to estimate the position after that. The magnetic and vision-aided navigation system is able to provide successful vision position

Table 5: Summary of simulation results.

Case	**Magnetic Navigation**	**Vision Navigation**		**Vision "Hits"**
		Config.	**Start Time (s)**	
1	Off	Observing	300	168
2	On	Observing	300	1,746
3	Off	Aiding	300	316
4	On	Aiding	300	3,929
5	Off	Aiding	1700	0
6	On	Aiding	1700	2,181

estimates for the length of the profile. Any vision outages observed are temporary with the magnetic navigation system reducing filter errors during those periods of time. Finally, cases 5 and 6 demonstrate that magnetic navigation is able to bound the INS drift over a long period of time with no computer vision data availability. When computer vision data becomes available, vision-aided navigation system is able to quickly provide a position estimate to the navigation filter. This was not achievable without the magnetic navigation system. Adding magnetic navigation to a vision-aided navigation system increases the reliability of the overall navigation system, and reduces the effects of vision outages on the system. The magnetic navigation system is able to bound the drift of the INS, and allow the vision-aided navigation system to provide position estimates as soon as computer vision data becomes available.

It is important to note that the magnetic navigation results in the simulations are demonstrated on synthetic magnetic field data. In these simulations, the navigation filter is able to perfectly remove the aircraft disturbance field from the synthetic measurements. The most challenging part of magnetic navigation on a real data set is compensating for the aircraft disturbance field. This problem becomes even more challenging on an operational aircraft such as the F-16, which is more dynamic and magnetically noisy than the aircraft used in previous magnetic navigation research. As demonstrated in the simulations, bounding the INS drift using magnetic navigation allows a course position estimate to be used for a vision-aided navigation system. This increases the likelihood of the vision-aided navigation system being able to provide a successful position estimate to the navigation filter. The next portion of research demonstrates magnetic navigation on an operational platform.

4.4 F-16 Flight Profiles

The magnetic navigation flight test data was collected for this work at the U.S. Air Force Test Pilot School (TPS) on an F-16 [45]. A majority of testing was flown near Edwards Air Force Base, California over high fidelity anomaly maps, as detailed in Section 3.7.2. Of 17 test flights that were executed, nine profiles were selected for this research and are summarized in Table 6. Each of the nine profiles consist of approximately one hour of flight within the boundaries of a magnetic anomaly map.

The first two profiles were flown at a level altitude, equal to that of the Cords Road anomaly map (1066 m). Profiles 3 and 4 were flown at a level altitude, equal to that of the Medium Altitude anomaly map (2134 m). Profiles 5 and 6 were flown at a level altitude 304 m (1,000 feet) above the Medium Altitude anomaly map. Each of the level altitude flights were flown within approximately 50 m of their target altitude. The last three profiles were flown at varying altitudes above the Medium Altitude anomaly map, with the purpose of exploring the use of magnetic anomaly maps in three dimensions. Flight profiles that were flown above anomaly map altitudes (profiles 5 through 9), were flown within the inner 60% of the map in an attempt to avoid errors in upward continuation filtering.

Table 6: Summary of F-16 flight profiles.

Profile	**Altitude, MSL (m)**	**Date**	**RADAR**	**Maneuvering**
1	1066	10 Sep 20	Off	Benign
2	1066	14 Sep 20	On	Benign
3	2134	10 Sep 20	Off	Benign
4	2134	15 Sep 20	On	Benign
5	2438	18 Sep 20	Off	Benign
6	2438	17 Sep 20	On	Benign
7	2134 - 5000	11 Sep 20	Off	Benign
8	2134 - 5000	16 Sep 20	Off	Dynamic
9	2134 - 5000	21 Sep 20	On	Dynamic

The aircraft RADAR and types of aircraft maneuvering were additional changes between flight profiles. The aircraft RADAR was varied to see if a high-power aircraft system had any affect on observed aircraft disturbance field. While RADAR analysis is beyond the scope of the research conducted in this report, it is noted to observe any data trends between the two configurations. Aircraft maneuvering was limited to benign maneuvering during a majority of the profiles—the aircraft was kept level to the best of the aircrew's ability unless a turn was required to stay within the anomaly map boundaries or for safety of flight. More dynamic maneuvering was performed on profiles 8 and 9 in an attempt to fly closer to how aircrew may fly operationally. Altitude changes and turns were more abrupt and level flight was not always a concern during the profile. More information on the flight test profiles can be found in [45].

Each profile is used to present the aircraft magnetic disturbance field of the F-16 in flight. Limited compensation was performed on each profile in an attempt to reduce the aircraft disturbance to levels which can be used for navigation. Only profile 1 was then used to demonstrate magnetic navigation on this operational aircraft based on the limited compensation that was conducted. Flight trajectories over the anomaly maps from profiles 1 and 7 are shown in Figure 36 and Figure 37.

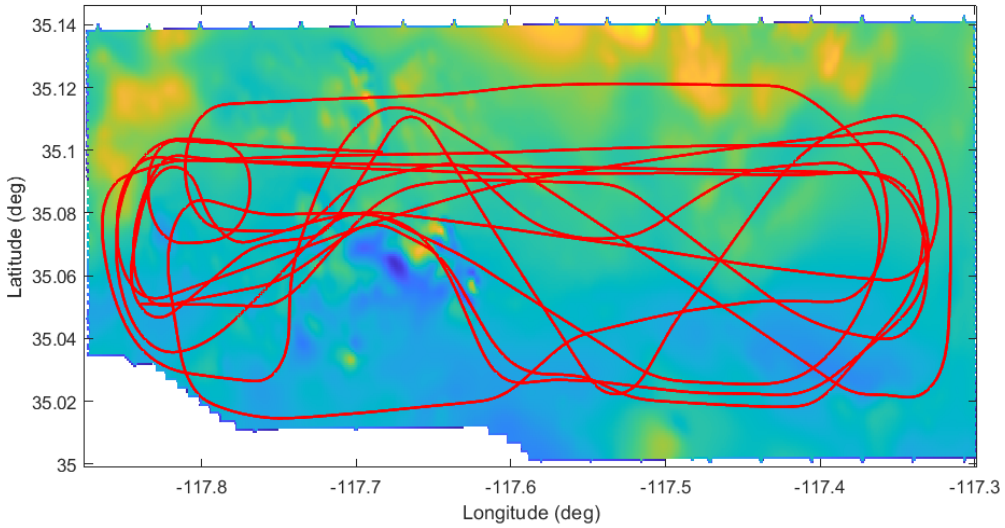

Figure 36: F-16 Profile 1: Flight trajectory over Cords Road magnetic anomaly map. Altitude was held level at the altitude of the anomaly map.

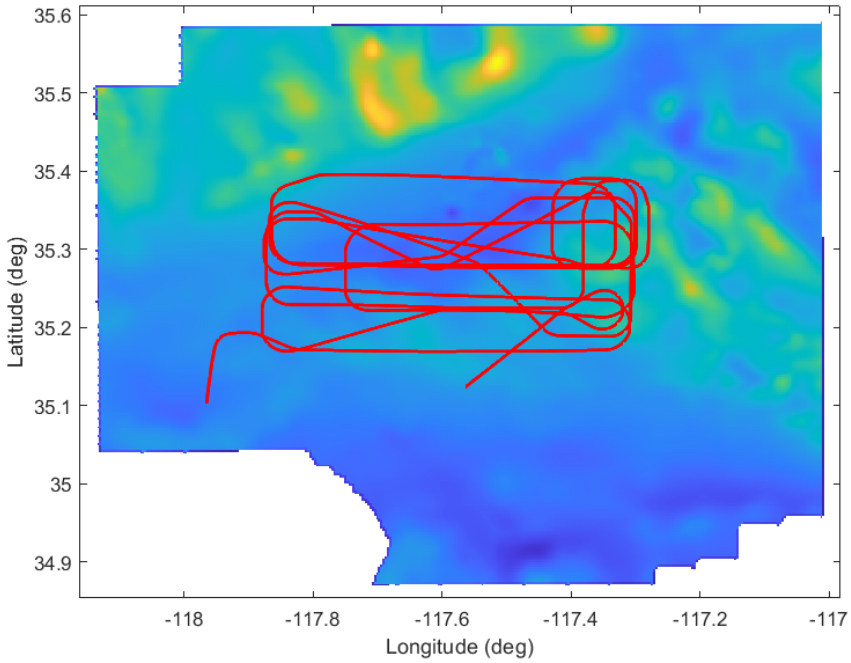

Figure 37: F-16 Profile 7: Flight trajectory over Medium Altitude magnetic anomaly map. Altitude was varied above the altitude of the anomaly map and flight was within the inner 60% of the map.

4.5 F-16 Aircraft Disturbance and Compensation

This section presents the aircraft disturbance field of the F-16 as measured during flight testing and the results of limited aircraft magnetic compensation efforts. The aircraft disturbance field data obtained during flight testing is for a single test configuration of the F-16, and it should not be assumed that all F-16 will have similar fields. Aircraft configuration and magnetometer placement are some of the most important factors for the aircraft disturbance field. Additionally, the compensation results presented in this research are limited. They are used primarily as a intermediary tool to demonstrate magnetic navigation on an F-16. There are some conclusions that can be made from the compensation results, but separate research efforts focusing on compensation such as [22] should be referenced for a better analysis.

4.5.1 F-16 Aircraft Disturbance In Flight

The aircraft disturbance field of the F-16 in flight is observed for each of the 9 profiles. An approximate disturbance field can be isolated from scalar magnetometer measurements by removing the Earth's main field and anomaly field using truth positioning information, the World Magnetic Model (WMM), and the magnetic anomaly map. The disturbance field for profile 1 is shown in Figure 38. The range of the field—the difference between absolute maximum and minimum values—is approximately 10,000 nano-Teslas (nT). Each flight profile resulted in similar disturbance field values. The absolute extrema and range are summarized in Table 7, rounded to the nearest 100 nT. The importance in compensating for the aircraft disturbance field can be seen by observing the combined magnetic intensity of the Earth's main field and anomaly field, which is shown in Figure 39 for profile 1. The magnetic intensity is debiased—the mean was removed—for better visual inspection. For navigation, the combined intensity—which is on the order of 100 nT—needs to be isolated in

flight from a measurement that contains 10,000 nT of disturbance. The 10,000 nT aircraft disturbance field for the flight test configuration of the F-16 is too large to compensate for using traditional compensation methods, such as those that employ the Tolles-Lawson model. Improved compensation methods, such as those that use machine learning, can be used to reduce the aircraft disturbance field enough for a demonstration of magnetic navigation.

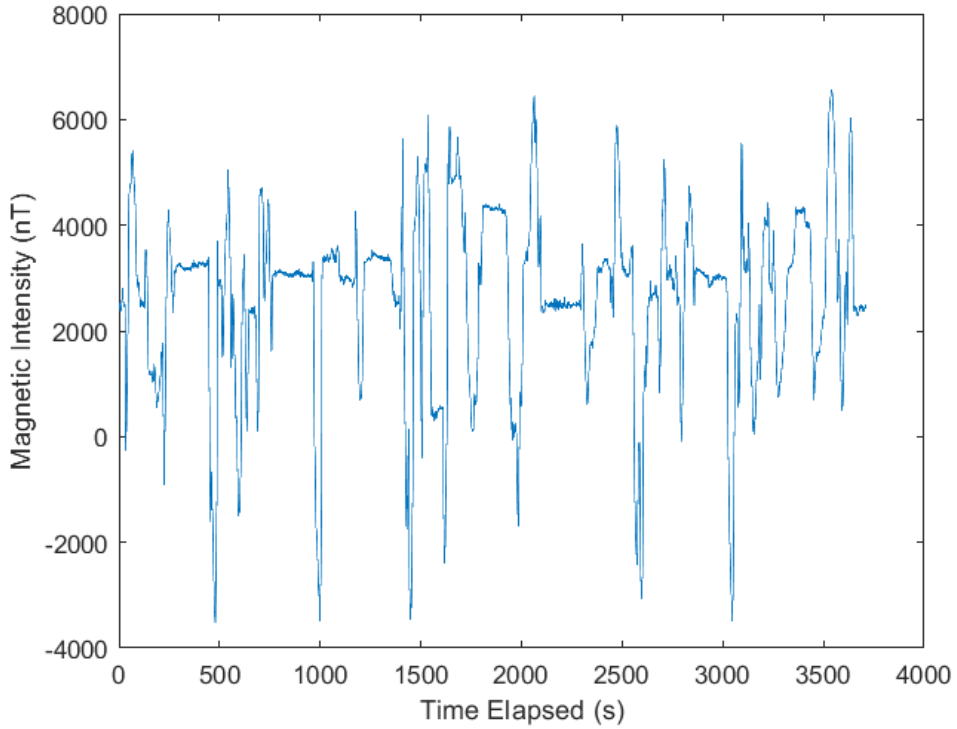

Figure 38: F-16 Profile 1: Scalar magnetic intensity of the aircraft disturbance field. The Earth's main field and anomaly field were removed from scalar magnetometer measurements in flight to approximate the aircraft disturbance field.

Table 7: Summary of F-16 aircraft disturbance in flight. Results rounded to the nearest 100 nT.

Profile	**Aircraft Disturbance (nT)**		
	Minimum	**Maximum**	**Range**
1	-3,500	6,500	10,000
2	-3,600	6,700	10,300
3	-3,500	6,900	10,400
4	-3,200	6,800	10,000
5	-3,000	6,900	9,900
6	-3,500	5,900	9,400
7	-3,400	7,000	10,400
8	-3,600	6,900	10,500
9	-3,400	6,900	10,300

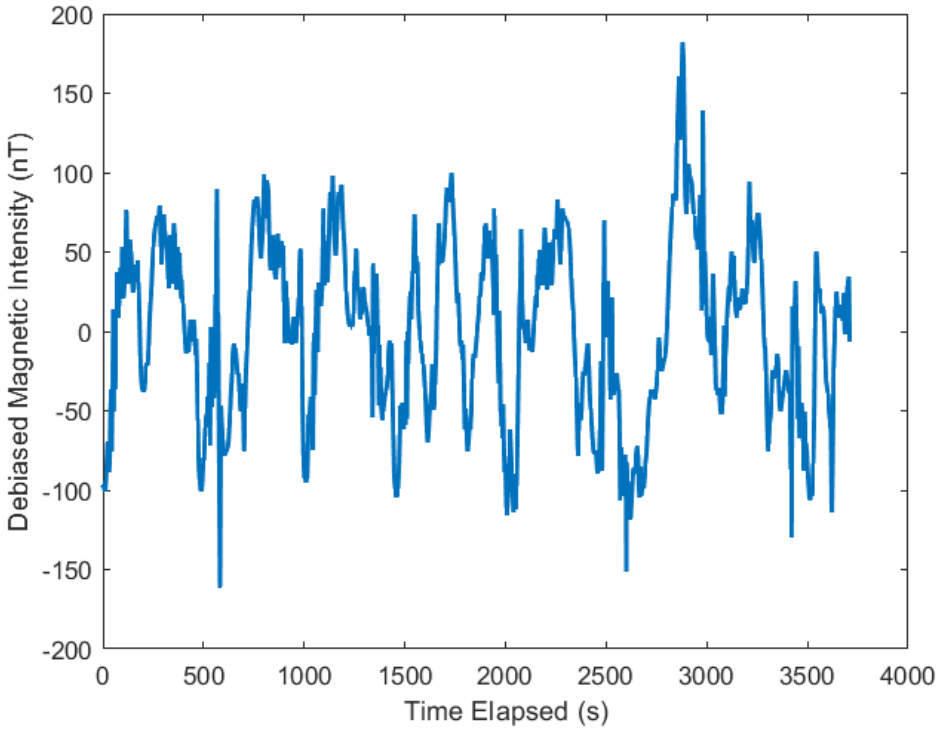

Figure 39: F-16 Profile 1: Combined magnetic intensity of the Earth's main field and anomaly field. The intensity is debiased for visual inspection.

4.5.2 Compensation of F-16 Aircraft Disturbance

A limited machine learning method was used to compensate for the aircraft disturbance field of the F-16, as detailed in Section 3.4.1. The 18 Tolles-Lawson parameters were used as inputs to the machine learning algorithm to model the expected scalar intensity of the combined main field and anomaly field. The first half of the profile was used as the training set to be run on the second half of the profile. The combined main field and anomaly field are shown in Figure 40 for the second half of profile 1 along with the neural network prediction from the machine learning algorithm. The neural network prediction successfully follows the trends of the combined main field and anomaly field, which proves promising for a magnetic navigation algorithm. The compensation error—difference between combined main and anomaly field and the neural network prediction—was used to assess compensation on the raw scalar magnetometer measurements. The compensation error for the second half of profile 1 is shown in Figure 41. The limited compensation approach was able to compensate a measurement with 10,000 nT of aircraft disturbance to within 10s of nT of error. The standard deviation of the compensation error presented for profile 1 is 16 nT.

Due to the inherent randomness present in machine learning, compensation algorithms were run for multiple trials. Ten compensation trials were performed on each flight profile. Compensation error was computed for each trial and the standard deviation of that error was calculated. The standard deviation results for profile 1 through 9 are summarized in Table 8. The minimum standard deviation is shown to reflect the best compensation result for that profile, and the maximum is shown to reflect the worst compensation result.

The machine learning compensation approach yields some similar results for most of the flight profiles as to that displayed in Figures 40 and 41 for profile 1. The minimum standard deviations—the best case compensation results—are between 10

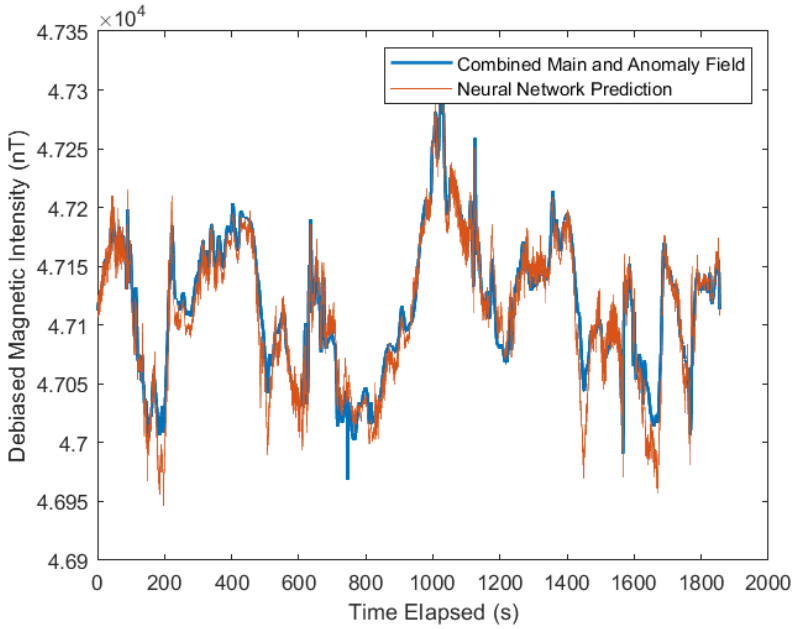

Figure 40: F-16 Profile 1: Combined main field and anomaly field compared to the neural network prediction for the second half of profile 1 using a limited machine learning approach to compensation.

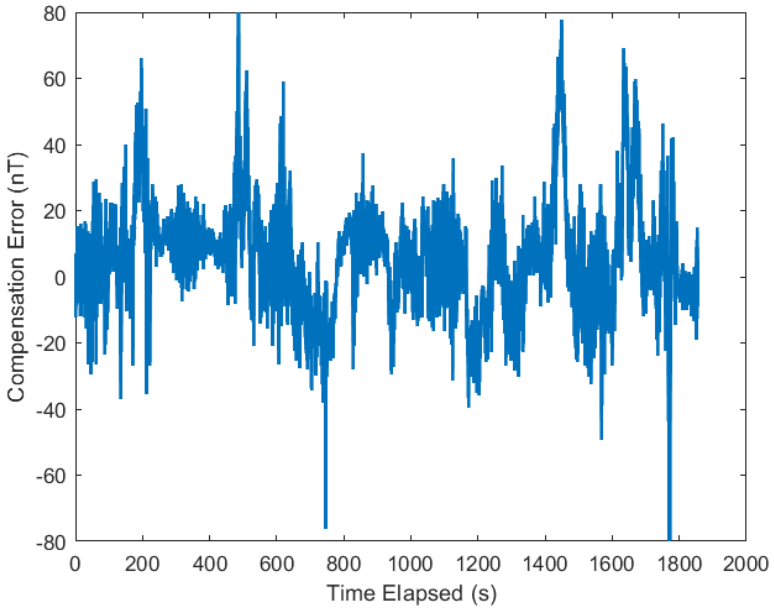

Figure 41: F-16 Profile 1: Aircraft magnetic compensation error for the second half of profile 1 using a limited machine learning approach to compensation.

Table 8: Summary of F-16 compensation error using a limited machine learning approach to compensation.

Profile	**Compensation Error Standard Deviation (nT)**		
	Minimum	**Maximum**	**Mean**
1	14	40	19
2	14	18	16
3	12	1,275	59
4	10	20	12
5	15	26	18
6	35	2,575	487
7	12	15	13
8	16	48	23
9	12	16	14

nT and 16 nT for all profiles except for profile 6. The poor results for case 6, the variation in maximum standard deviations, and the range between minimums and maximums are characteristic of the limited nature of the compensation method used. Magnetic compensation on an operation platform such as the F-16 is a separate focus of study to this research. More information on the topic can be found in [21] and compensation results from the same F-16 data set can be found in [22]. The limited compensation results are presented here as a means to achieve at least one working result to be used for a demonstration of magnetic navigation on an F-16.

4.6 F-16 Magnetic Navigation Results

Magnetic navigation is demonstrated on the F-16 using the result of the limited magnetic compensation on the second half of flight profile 1. Only profile 1 is examined, and the same trial that is presented in Figures 40 and 41 is used for navigation. Results are presented for both a navigation grade INS and a tactical grade INS. The second half of profile 1 was approximately 1,800 seconds (30 minutes). Filter tuning on profile 1's compensation error resulted in a σ_{FOGM} of 15 nT and τ_{FOGM} of 20

seconds. These values are used to model the first-order Gauss Markov (FOGM) state within the navigation filter for both INS models. The navigation filter was initialized at the truth position, velocity, and attitude with initial position uncertainty of 5 m, velocity uncertainty of 0.1 m/s, and attitude uncertainty of 0.01 deg.

4.6.1 Navigation Grade INS

The F-16 magnetic navigation results using a navigation grade INS are shown in Figure 42. The navigation filter is able to successfully bound the navigation solution and prevents the drift that would be seen with an INS-only solution. Position errors in both the North and East channels are approximately 100 meters upon visual inspection. This compares to the approximate 1 nautical mile (1,850 meters) per hour drift that would be seen with a navigation grade INS. The resulting measurement variance R from filter tuning was 30^2 nT. Since synthetic IMU measurements are used to produce the navigation solution, 10 trials were executed to generate 10 different realizations of those measurements. Each realization is shown in gray in Figure 42. This allows us to confirm how similar results are for each IMU measurements realization. Each of the 10 IMU realizations produced a similar bounded navigation solution for profile 1, indicating that the navigation filter is tuned adequately. A top-down view of the navigation filter solution compared to the truth trajectory is shown in Figure 43.

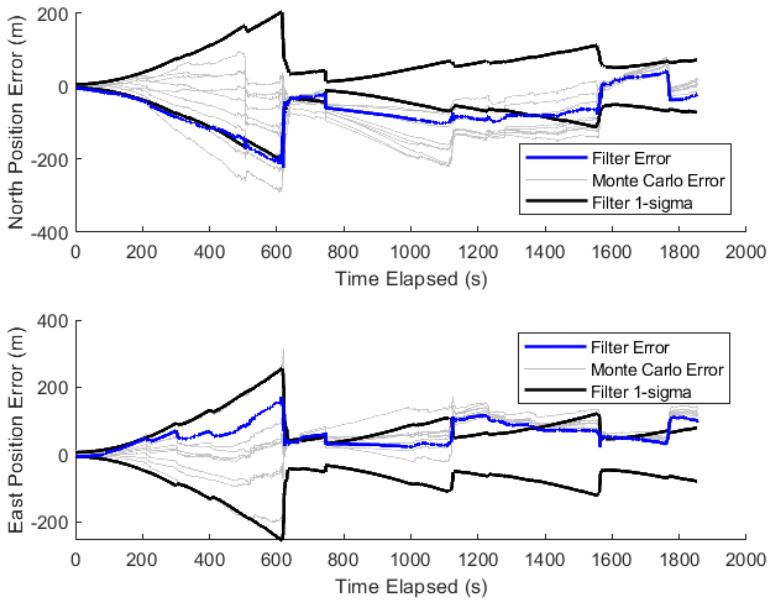

Figure 42: F-16 Profile 1: Magnetic navigation position error with navigation grade INS for the second half of profile 1. 10 Monte-Carlo trials are shown in gray for 10 different realizations of the synthetic IMU measurements. The trial in blue is shown in the following figure.

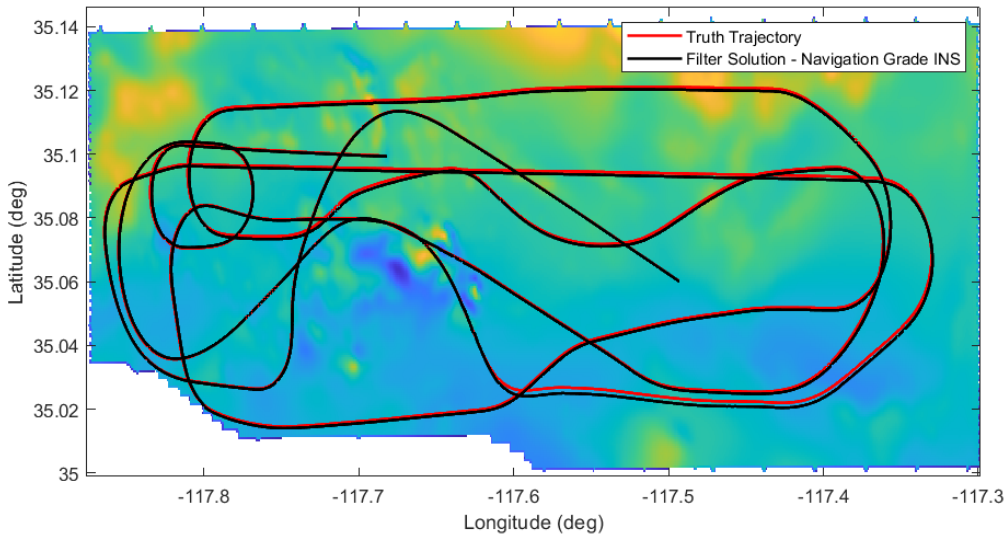

Figure 43: F-16 Profile 1: Top-down view of magnetic navigation solution with a navigation grade INS compared to the truth trajectory. Results are for the second half of profile 1. Each realization of synthetic IMU measurements produced similar results to that shown.

4.6.2 Tactical Grade INS

The navigation results using a tactical grade INS are shown in Figure 44. Tactical grade INS drift can be greater than 10 nautical miles (18,500 meters) per hour. The navigation filter is again able to successfully bound the navigation solution, and position errors are kept below approximately 500 meters upon visual inspection. The resulting measurement variance R from filter tuning was 100^2 nT. Again, since synthetic IMU measurements are used to produce the navigation solution, 10 trials were executed to generate 10 difference realizations of those measurements. Each of the 10 IMU realization trials is used in a navigation solution and are shown in gray in Figure 44. Trial results were not as conclusive as the navigation grade INS results, indicating that the navigation filter could use additional filter tuning. 3 out of 10 trials resulted in a bounded navigation solution that did not diverge. A top-down view of one of these solutions compared to the truth trajectory is shown in Figure 45. 5 out of 10 trials resulted a bounded navigation solution for the first 1500 seconds before diverging. An example of for those trials is shown in Figure 46. 2 out of 10 trials resulted in a filter divergence at approximately 600 seconds, taking the navigation solution off of the magnetic anomaly map where it is unlikely able to return to a bounded solution. An example for those trials is shown in Figure 47. Additional filter tuning with the tactical grade INS may be able to increase the number of bounded navigation solutions, but since the tuned value of the measurement variance R is already so large (100^2 nT), a closer look at the divergences is required.

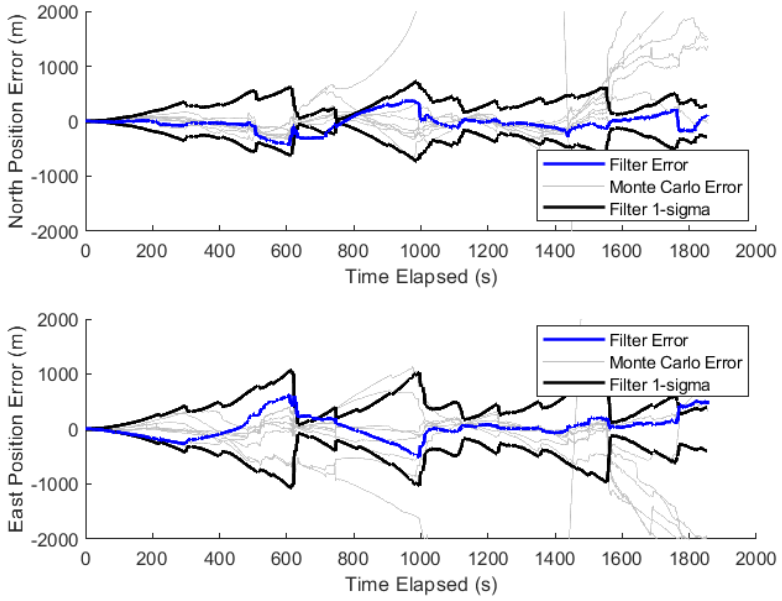

Figure 44: F-16 Profile 1: Magnetic navigation position error with tactical grade INS for the second half of profile 1. 10 Monte-Carlo trials are shown in gray for 10 difference realizations of the synthetic IMU measurements. The trial in blue in shown in the following figure.

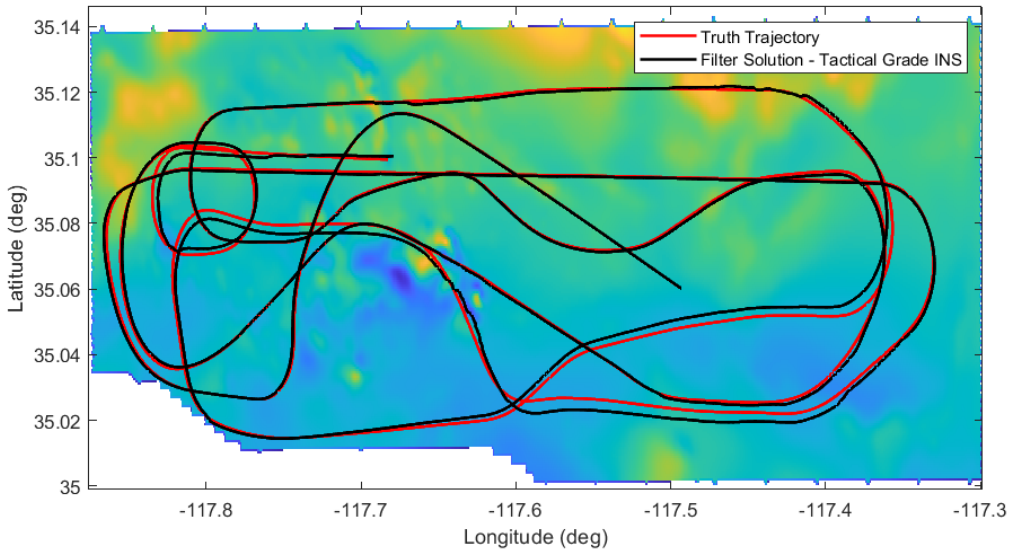

Figure 45: F-16 Profile 1: Top-down view of successful magnetic navigation solution with a tactical grade INS compared to the truth trajectory. Results are for the second half of profile 1. 3 of 10 realization trials of synthetic IMU measurements produced similar results to that shown.

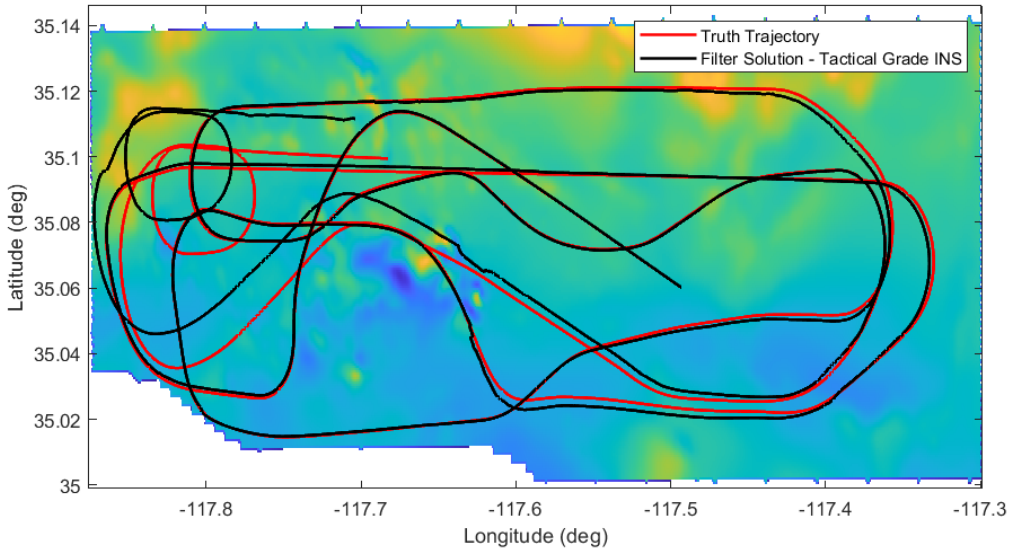

Figure 46: F-16 Profile 1: Top-down view of degraded magnetic navigation solution with a tactical grade INS compared to the truth trajectory. Results are for the second half of profile 1. 5 of 10 realization trials of synthetic IMU measurements produced similar results to that shown.

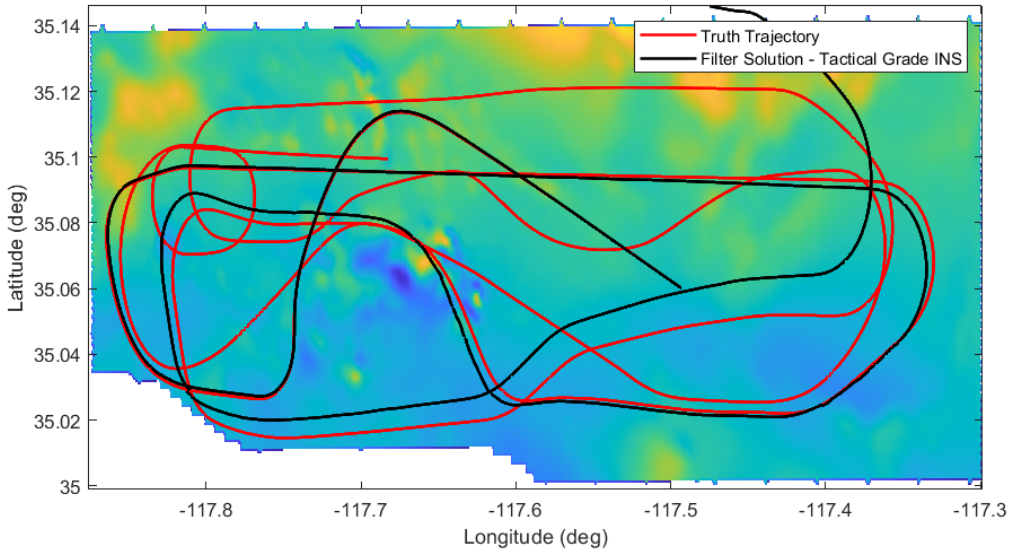

Figure 47: F-16 Profile 1: Top-down view of diverged magnetic navigation solution with a tactical grade INS compared to the truth trajectory. Results are for the second half of profile 1. 2 of 10 realization trials of synthetic IMU measurements produced similar results to that shown.

The North position error is repeated again in Figure 48. The time periods when the two groups of divergences occur are marked with vertical lines. These are at approximately 600 seconds and 1500 seconds. Also shown in Figure 48 are the debiased expected measurement (combined main field and anomaly field with mean removed) and the compensation error. Both time periods when the divergences occur contain a reduction in the filter standard deviation. In magnetic navigation, this characteristic is typically seen when a large variation in magnetic anomaly is observed. This is confirmed in Figure 48, where we can see a highly variable expected measurement (plotted in the color blue) aligned with the standard deviation reduction during those periods. In those instances, we would expect the filter error to be reduced and not diverge. Looking at the compensation error (plotted in the color red) during both divergence time periods, there are no significant increases. Therefore, there are no indications that poor compensation caused the divergences in these instances. Another cause of divergences could be a multi-modal area on the anomaly map that the extended Kalman filter (EKF) is unable to handle well. The flight trajectory over the anomaly map is shown again in Figure 49. The divergence time periods are marked in black on the trajectory. We can see that both divergences occur over the same area of the anomaly map. This area includes highly variable anomalies and sharp multi-modal characteristics. This is a multi-modal scenario that EKFs do not handle well. It is suspected that a particle filter—which are better suited for the multi-modal characteristics of map-based navigation—would perform better during this navigation profile.

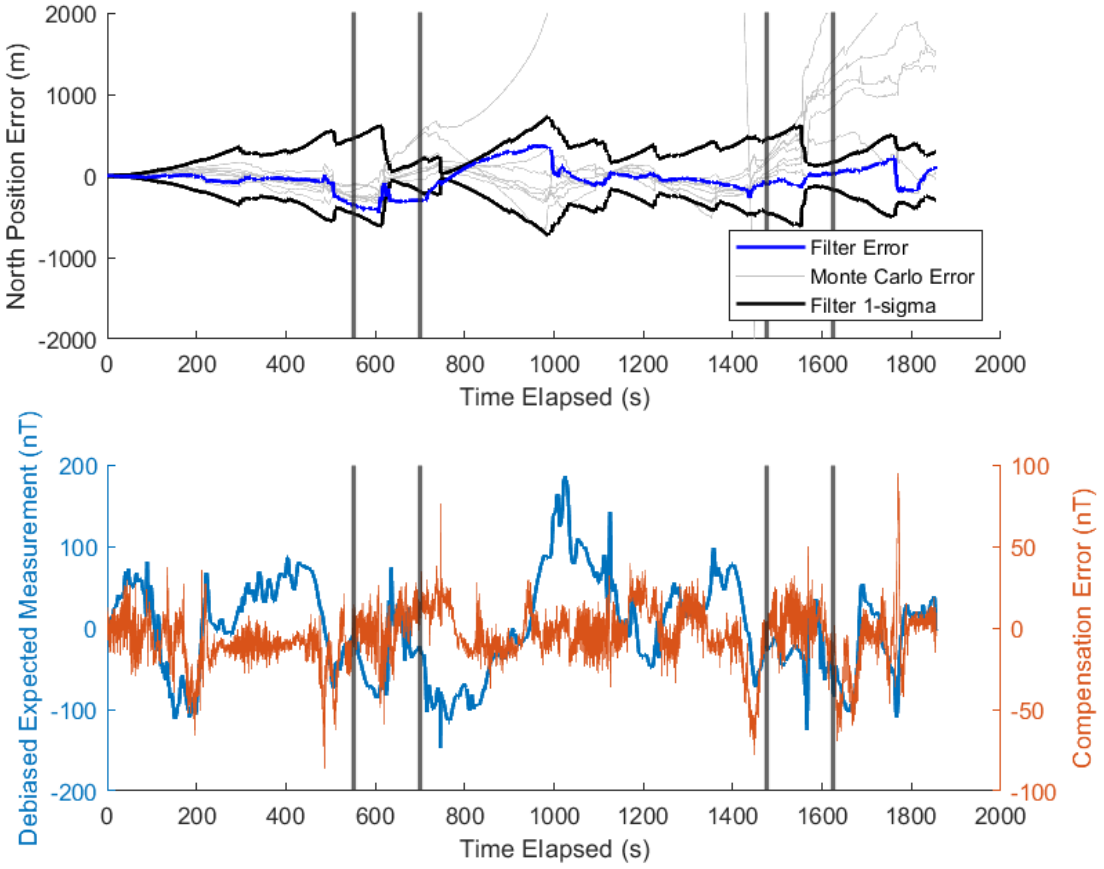

Figure 48: F-16 Profile 1: Divergence analysis on navigation solution with tactical grade INS. Results are for the second half of profile 1. North position error is shown on the top. The expected measurement (combined main and anomaly fields) and compensation error are shown on the bottom. Divergence time periods are marked with vertical lines.

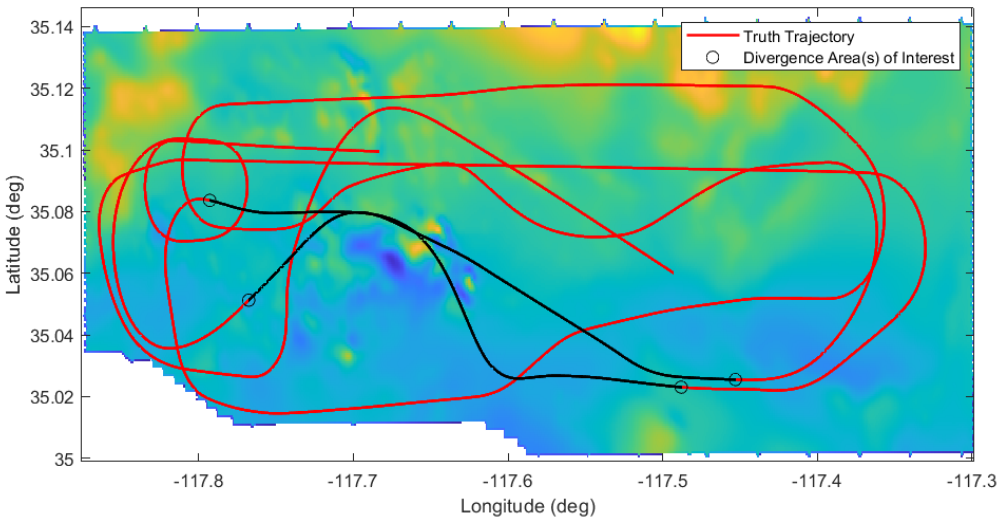

Figure 49: F-16 Profile 1: Top-down view of flight trajectory over the magnetic anomaly map. Results are for the second half of profile 1. Divergence time periods are marked in black. The divergences occur over an area of map with sharp multi-modal characteristics, which the EKF does not handle well.

4.7 F-16 Results Summary

The results from the nine F-16 flight profiles were presented to demonstrate magnetic navigation on a dynamic and operational aircraft. Aircraft disturbance observation, magnetic compensation, and magnetic navigation were all successfully demonstrated for the F-16.

The large aircraft disturbance field is observed for nine flight test profiles. The disturbance field had a range of approximately 10,000 nT for each flight test profile. Comparing this to the combined intensity of the Earth's main field and anomaly field for the duration of the flight profile, which is on the order of 100 nT, proves the need for compensating for disturbance. A limited approach to magnetic compensation demonstrated an effective compensation result. A machine learning algorithm was trained on the first half of the flight profile using the Tolles-Lawson parameters as inputs and the combined intensity of the Earth's main and anomaly fields as the output. The compensation method was able to reduce the 10,000 nT aircraft disturbance field down to 10s of nT of compensation error for a majority of the flight test profiles. A more focused effort on magnetic compensation of the aircraft disturbance in dynamic platforms should be conducted to optimize the results. [22] begins to looks at compensation of the same F-16 magnetic field data set.

Using the compensation results for the second half of test profile 1, magnetic navigation was demonstrated on the F-16. Both navigation grade and tactical grade IMU measurements were generated for the data set and navigation solutions were computed for each. With a navigation grade INS, F-16 magnetic navigation resulted in a bounded navigation solution for the second half of the profile. Position errors were approximately 100 meters. For the tactical grade INS, F-16 magnetic navigation resulted in a bounded navigation solution for 3 out of 10 Monte-Carlo trials. Position errors were approximately 1,000 meters. Results indicated that reliability of the

navigation filter with a tactical grade INS could be improved by using a marginalized particle filter instead of an EKF. Achieving a bounded navigation solution on the F-16 using magnetic navigation demonstrates there is promise in combining this alternative navigation method with a vision-aided navigation system. As shown in Section 4.2, a magnetic navigation system can bound the INS drift during periods of computer vision outages and allow vision-aided navigation to continue once vision data is available. More optimized compensation methods and navigation filters can potentially produce better results and allow a real-time solution to be computed for magnetic and vision-aided navigation.

V. Conclusion

This chapter presents the conclusions and findings from this research and discusses future work to improve a navigation system that combines magnetic and vision-aided navigation as an alternative navigation method. This research first sought to demonstrate a real-time magnetic and vision-aided navigation system using synthetic magnetic field measurements and flight test gathered computer vision data. Second, this research sought to demonstrate that a bounded navigation solution can be achieved on a dynamic operational aircraft using a magnetic navigation system and limited aircraft magnetic compensation methods. This bounded navigation solution could then potentially be combined with a vision-aided navigation system.

5.1 Research Conclusions

Based on the results from simulation cases, a real-time magnetic and vision-aided navigation system can bound inertial navigation system (INS) drift and produce a high accuracy navigation solution without the presence of Global Positioning System (GPS) over an area that contains known aerial imagery with accurate landmark coordinates. A magnetic navigation system can bound INS drift and provide a course navigation solution. This course solution can be combined with a vision-aided navigation solution to allow initialization of the vision-navigation system after periods of computer vision outages. A prime example of a computer vision outage is when images with known landmark coordinates are unavailable or when images contain poor features, such as flight over a body of water. The research conducted on the simulations used a black box vision-aided navigation system. Conclusions on how accurate of a magnetic navigation solution are needed to initialize the vision-aided navigation system could not be made. Those results are dependent on which vision-navigation

system is chosen and how it interacts within the navigation filter.

F-16 magnetic navigation results demonstrated that magnetic navigation is achievable on a dynamic and operational aircraft. Large aircraft disturbances can be present on aircraft that are not optimized for magnetic navigation, as was present on the F-16. A limited magnetic compensation approach was able to compensate for the large aircraft disturbance present in the magnetic field measurements and produce an output usable in the magnetic navigation system. The magnetic navigation system was able to bound the navigation solution when aiding both a navigation grade and tactical grade INS. This research cannot conclude whether the bounded navigation solution is accurate enough to initialize a theoretical vision navigation system. Since the compensation methods used were limited and not an optimized solution, the navigation solution obtained can be improved.

5.2 Recommendations for Future Work

Results obtained with this research show promise for magnetic navigation on dynamic platforms, and for combining magnetic navigation with a vision-aided navigation system when GPS is not available. Additional research and testing is required on both magnetic navigation and vision-aided navigation systems.

For vision-aided navigation systems such as the absolute positioning system used in this research, additional research can quantify how accurate of a navigation solution is required to initialize a vision navigation system. Those results set a target for the accuracy of a magnetic navigation solution. For magnetic navigation, research must still be done on magnetic compensation on a dynamic aircraft with a large aircraft disturbance field. Ideally, magnetic navigation would be used on a platform that is specifically designed around reducing the aircraft disturbance seen by the sensors. After that is done, or if that cannot be done, then compensation algorithms need to be

able to be able to reduce thousands of nano-Teslas of disturbance. The compensation method used in this research did not attempt to perform pre-flight compensation using a calibration flight, the inputs to the algorithm were not experimented with nor optimized, nor were F-16 aircraft states included in compensation at any time. The F-16 flight test data set gathered by the U.S. Air Force Test Pilot School (TPS) can be used to explore all of these avenues plus many more to further the field of magnetic navigation. Lastly, additional research and testing can be conducted to test that both magnetic navigation and vision-aided navigation systems are functional together to produce a real-time navigation solution on a dynamic platform.

Bibliography

1. Canciani, Aaron. *Absolute Positioning Using the Earth's Magnetic Anomaly Field*. Dissertation, Air Force Institute of Technology, 2016.

2. Venable, Donald. *Improving Real World Performance for Vision Navigation in a Flight Environment*. Dissertation, Air Force Institute of Technology, 2016.

3. Wilson, John M. and Kline-Schoder, Robert J. Passive navigation using local magnetic field variations. *ION NTM*, 2006.

4. Malec, Michael. *Airborne Magnetic Anomaly Navigation Over Ocean Using Under Sample Maps*. Thesis, Air Force Institute of Technology, 2018.

5. Mount, Lauren. *Navigation using Vector and Tensor Measurements of the Earth's Magnetic Anomaly Field*. Thesis, Air Force Institute of Technology, 2018.

6. Lee, Taylor. *Aerial Simultaneous Localization and Mapping Using Earth's Magnetic Anomaly Field*. Thesis, Air Force Institute of Technology, 2019.

7. European Space Agency. Magnetic Field Sources. `http://www.esa.int/spaceinimages/Images/2012/10/Magnetic_field_sources`. [Online; accessed Oct-2019].

8. Hinze, William J. and Frese, R. Von and Saad, Afif H. *Gravity and Magnetic Exploration: Principles, Practices, and Applications*. Cambridge University Press, 2012.

9. Reeves, Colin. *Aeromagnetic Surveys: Principles, Practice and Interpretation*. Geosoft, 2005.

10. Hulot, G. and Balogh, A. and Christensen, U.R. and Constable, C. and Mandea, M. and Olsen, N. *Terrestrial Magnetism (Space Sciences Series of ISSI)*. Springer, 2011.

11. North American Space Agency. Measuring Earth's Magnetism. `https://earthobservatory.nasa.gov/images/84266/measuring-earths-magnetism`. [Online; accessed Oct-2019].

12. Cain, Joseph and Blakely, Richard. The magnetic field of the earth's lithosphere: The satellite perspective. *EOS Transactions*, 80:156–156, 04 1999.

13. Meyer, Brian and Saltus, Richard and Chulliat, Arnaud. EMAG2v3: Earth Magnetic Anomaly Grid (2-arc-minute resolution). Version 3. NOAA National Centers for Environmental Information. `https://doi.org/10.7289/V5H70CVX`. [Online; accessed Oct-2019], 2017.

14. National Oceanic and Atmospheric Administration. EMAG2: Earth Magnetic Anomaly Grid (2-arc-minute resolution). `https://ngdc.noaa.gov/geomag/emag2.html`. [Online; accessed Oct-2019].

15. INTERMAGNET. `http://www.intermagnet.org/data-donnee/data-eng.php`. [Online; accessed Oct-2019].

16. National Oceanic and Atmospheric Administration. Geomagnetic Data and Information - The World Magnetic Model. `https://ngdc.noaa.gov/geomag/WMM/DoDWMM.shtml`. [Online; accessed Oct-2019].

17. Reid, A. B. Aeromagnetic survey design. *Geophysics*, 45:973, May 1980.

18. Bankey, Viki and Cuevas, Alejandro and Daniels, David and Finn, Carol A. and Hernandez, Israel and Hill, Patricia and Kucks, Robert and Miles, Warner and

Pilkington, Mark and Roberts, Carter and Roest, Walter and Rystrom, Victoria and Shearer, Sarah and Snyder, Stephen and Sweeney, Ronald and Velez, Julio and Phillips, J.D. and Ravat, D. Digital data grids for the magnetic anomaly map of north america: U.s. geological survey open-file report 02-414. *U.S. Geological Survey*, 2002.

19. Blakely, Richard J. *Potential Theory in Gravity and Magnetic Applications*. Cambridge University Press, 1996.

20. Sander Geophysics Limited. `http://sgl.com/MagTF.html`. [Online; accessed Jan-2021].

21. Hezel, Mitchel. *Improving Aeromagnetic Calibration Using Artificial Neural Networks*. Thesis, Air Force Institute of Technology, 2020.

22. Emery, Kyle. *Improving Aeromagnetic Calibration by Mixing Artificial Neural Networks and Tolles-Lawson - M.A.N.N.T.L.* Thesis, Air Force Institute of Technology, 2021.

23. Woloszyn, Miroslaw. Analysis of aircraft magnetic interference. *International Journal of Applied Electromagnetics and Mechanics, 39(1-4):129-136*, 2012.

24. Tolles, W. E. and Lawson, J. D. . *Magnetic Compensation of MAD Equipped Aircraft*. Airborne Instruments Lab Inc., Mineola, NY, 1950.

25. Mandea, Mioara and Korte, Monika. *Geomagnetic Observations and Models*. Springer Science and Business Media, 2010.

26. Scaramuzza, David and Fraundorfer, Friedrich. Visual odometry part 1: The first 30 years and fundamentals. *Robotics and Automation Magazine*, (December):80—92, 2011.

27. Freidel, Zachary. *Event-Based Visual-Inertial Odometry Using Smart-Features*. Thesis, Air Force Institute of Technology, 2020.

28. Raquet, John. Alternative Navigation Lecture Slides, Winter Quarter, 2019.

29. Open Source Computer Vision (openCV) Documentation - solvePnP() Function. `https://docs.opencv.org/3.4.2/index.html`. [Online; accessed Jan-2021].

30. OpenCV Documentation - Harris Corner Detector Tutorial. `https://docs.opencv.org/3.4.2/d4/d7d/tutorial_harris_detector.html`. [Online; accessed Jan-2021].

31. Scaramuzza, David and Fraundorfer, Friedrich. Visual odometry part 2: Matching, robustness, and applications. *Robotics and Automation Magazine*, June:78—90, 2012.

32. Harris, C. and Pike, J. 3d positional integration from image sequences. *Alvey Vision Conference*, 1988.

33. Tomasi, C. and Shi, J. Good features to track. *CVPR'94*, pages 593—600, 1994.

34. Lowe, D. Distinctive image features from scale-invariant keypoints. *International Journal of Computer Vision*, volume 20:91—110, 2003.

35. Bay, H. and Tuytelaars, T. and Van Gool, L. Surf: Speeded up robust features. *ECCV*, pages 404—417, 2006.

36. Fischler, M.A. and Bolles, R.C. Ransac random sampling concensus: A paradigm for model fitting with applications to image analysis and automated cartography. *Communication of ACM*, volume 26:381—395, 1981.

37. Hartley, R. and Zisserman, A. *Multiple View Geometry in Computer Vision, Volume 2*. Cambridge University Press, 2000.

38. Maybeck, Peter S. *Stochastic Models, Estimation, and Control, Volume 2*. Academic Press, Inc, New York, NY, 1979.

39. Titterton, David and Weston, John. *Strapdown Inertial Navigation Technology, 2nd Edition*. Electromagnetics and Radar Series, Institution of Engineering and Technology, 2004.

40. Autonomy and Navigation Technology Center. Scorpion Documentation. Air Force Institute of Technology, 2019.

41. Ohio Statewide Imagery Program. `https://ogrip.oit.ohio.gov/ProjectsInitiatives/StatewideImagery.as`. [Online; accessed Jun-2019].

42. Veth Research Associates. Image Positioning System for AgilePod PNT. Accessible via AFRL/RYWN.

43. Beale, Mark Hudson and Hagan, Martin T. and Demuth, Howard B. *Reference: Deep Learning Toolbox*. The Mathworks, Inc, Natick, MA, 2020.

44. U.S. Air Force Photo, David Dixon. `https://www.wpafb.af.mil/News/Article-Display/Article/1215444/afrls-cutting-edge-isr-platform-commences-harvest-reaper-flight-testing/`. [Online; accessed Nov-2019].

45. Clarke, Daniel and Soeder, Justin and Duncan, Raina and Ames, Christopher and Horgan, Casey and Turner, Bryce. A Limited Evaluation of Magnetic Anomaly Navigation, Project HAVE MANTA RAY. Technical Report USAFTPS-TIM-20A-02, U.S. Air Force Test Pilot School, Edwards AFB, CA, 2020.

46. Bates, Martin and Sirohey, Aamna. Aeromagnetic Navigation for U.S. Air Force Institute of Technology. Technical Report 880-2019-000, Sander Geophysics Limited, Ontario, ON Canada, 2019.

Acronyms

AFIT the Air Force Institute of Technology. 5, 38, 40

AFRL Air Force Research Laboratory. 45, 62

ANT Autonomy and Navigation Technology. 38

AWGN additive white Gaussian noise. 35, 42, 44, 45

COTS commercial off-the-shelf. 6

CRM Consejo de Recursos Minerales of Mexico. 14

DCM direction cosine matrix. 47

DRMS Distance Root Mean Square. 5, 6

EKF extended Kalman filter. iv, 5, 6, 40, 96, 99

EMAG Earth Magnetic Anomaly Grid. 8

FOGM first-order Gauss Markov. 21, 38, 41, 43, 44, 60, 90

GPS Global Positioning System. iv, 1, 2, 3, 4, 5, 14, 25, 46, 62, 64, 70, 71, 73, 74, 76, 77, 101, 102

GSC Geological Survey of Canada. 14

IMU inertial measurement unit. 2, 38, 40, 41, 54, 59, 62, 69, 91, 93, 99

INS inertial navigation system. iv, 1, 5, 6, 25, 36, 38, 40, 46, 62, 64, 70, 71, 73, 74, 75, 78, 80, 81, 90, 91, 93, 96, 99, 101, 102

NAMAD North American Magnetic Anomaly Database. 11, 14, 15, 49, 65

NCEI National Centers for Environmental Information. 10

NED North, East, and down. 47, 48

NGA National Geospatial-Intelligence Agency. 10

nT nano-Teslas. iv, 48, 85

PnP Perspective-N-Point. vii, 32, 33

PNT positioning, navigation, and timing. 62

RANSAC random sample consensus. 31

SIFT scale invariant feature transform. 29, 30, 31

SLAM simultaneous localization and mapping. 6

SURF speeded up robust features. 29, 30, 31

TPS Test Pilot School. 64, 82, 102

UAV unmanned aerial vehicle. 6

USGS United States Geological Survey. 14

WMM World Magnetic Model. 7, 10, 43, 47, 85

REPORT DOCUMENTATION PAGE

Form Approved
OMB No. 0704–0188

1. REPORT DATE *(DD–MM–YYYY)*	2. REPORT TYPE	3. DATES COVERED *(From — To)*
25–03–2021	Master's Thesis	Sept 2018 — Mar 2021

4. TITLE AND SUBTITLE

Real-Time Aerial Magnetic
And Vision-Aided Navigation

5a. CONTRACT NUMBER

5b. GRANT NUMBER

5c. PROGRAM ELEMENT NUMBER

6. AUTHOR(S)

Daniel J. Clarke

5d. PROJECT NUMBER

5e. TASK NUMBER

5f. WORK UNIT NUMBER

7. PERFORMING ORGANIZATION NAME(S) AND ADDRESS(ES)

Air Force Institute of Technology
Graduate School of Engineering and Management (AFIT/EN)
2950 Hobson Way
WPAFB OH 45433-7765

8. PERFORMING ORGANIZATION REPORT NUMBER

AFIT-ENG-MS-21-M-022

9. SPONSORING / MONITORING AGENCY NAME(S) AND ADDRESS(ES)

Intentionally Left Blank

10. SPONSOR/MONITOR'S ACRONYM(S)

11. SPONSOR/MONITOR'S REPORT NUMBER(S)

12. DISTRIBUTION / AVAILABILITY STATEMENT

DISTRIBUTION STATEMENT A:
APPROVED FOR PUBLIC RELEASE; DISTRIBUTION UNLIMITED.

13. SUPPLEMENTARY NOTES

14. ABSTRACT

Aerial magnetic navigation has shown to be a viable alternative navigation method that has the potential for world-wide availability, to include over oceans. Obtaining GPS-level accuracy using magnetic navigation alone is challenging, but magnetic navigation can be combined with other alternative navigation methods that are more posed to obtaining GPS-level accuracy in their current state. This research presents an aerial navigation solution combining magnetic navigation and vision-aided navigation to aid an inertial navigation system (INS). The navigation solution was demonstrated in real-time playback using simulated magnetic field measurements and flight-test captured visual imagery. Additionally, the navigation solution was flight-tested on a USAF F-16 to demonstrate magnetic navigation in the challenging magnetic environment seen on operationally representative dynamic platforms.

15. SUBJECT TERMS

Magnetic Navigation, Vision-Aided Navigation, Vision Navigation

16. SECURITY CLASSIFICATION OF:			17. LIMITATION OF ABSTRACT	18. NUMBER OF PAGES	19a. NAME OF RESPONSIBLE PERSON
a. REPORT	b. ABSTRACT	c. THIS PAGE			Captain Daniel J. Clarke, AFIT/ENG
U	U	U	UU	122	19b. TELEPHONE NUMBER *(include area code)* (937) 255-3636; daniel.clarke.11@us.af.mil